AD-A093 688 STANFORD UNIV CA EDWARD L GINZTON LAB OF PHYSICS F/G 20/5
TUNABLE OPTICAL SOURCES.(U)
NOV 80 R L BYER DAAG29-79-C-0181
UNCLASSIFIED GL-3209 ARO-15278.11-P NL

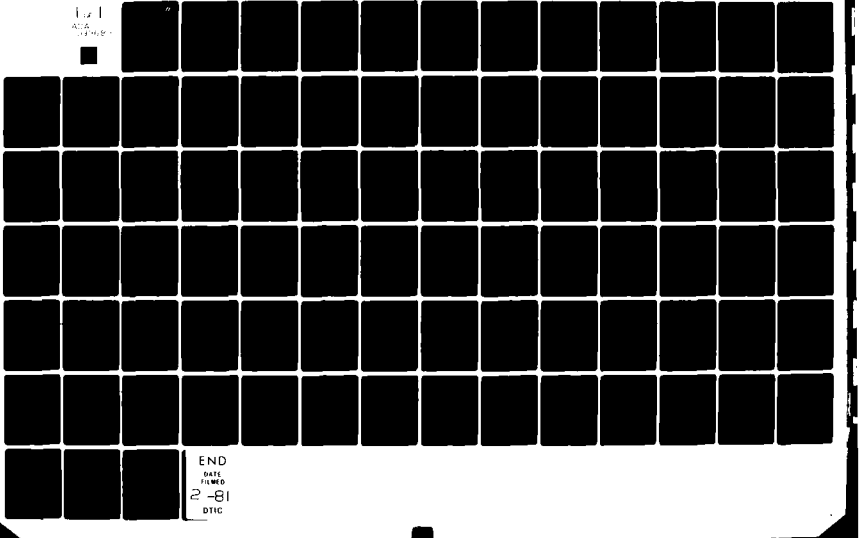

END
DATE FILMED
2-81
DTIC

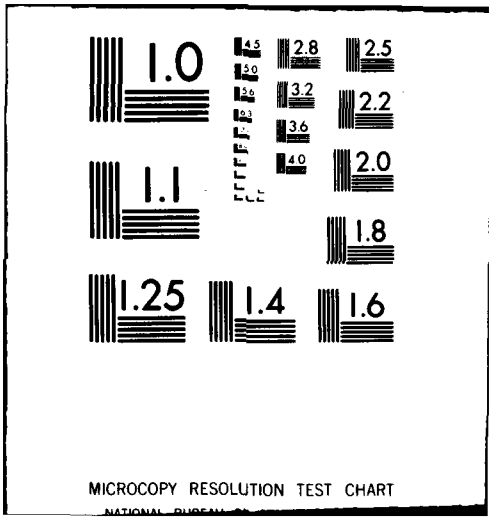
1.0
1.1
1.25
1.4
1.6
1.8
2.0
2.2
2.5
2.8
3.2
3.6
4.0
4.5
5.0
5.6
MICROCOPY RESOLUTION TEST CHART

TUNABLE OPTICAL SOURCES

Final Report

~~for the period~~

1 September 1979 - 31 August 1980

Robert L. Byer

November 1980

U.S. ARMY RESEARCH OFFICE

Contract: DAAG29-79-C-0181

Edward L. Ginzton Laboratory
Stanford University
Stanford, California 94305

Approved for Public Release;
Distribution Unlimited

The views, opinions, and/or findings contained in this report are those of the author(s) and should not be construed as an official Department of the Army position, policy, or decision, unless so designated by other documentation.

UNCLASSIFIED

SECURITY CLASSIFICATION OF THIS PAGE (When Data Entered)

REPORT DOCUMENTATION PAGE		READ INSTRUCTIONS BEFORE COMPLETING FORM
1. REPORT NUMBER	2. GOVT ACCESSION NO. AD-A093 688	3. RECIPIENT'S CATALOG NUMBER
4. TITLE (and Subtitle) TUNABLE OPTICAL SOURCES		5. TYPE OF REPORT & PERIOD COVERED Final Report 9.1.79 – 8.31.80
		6. PERFORMING ORG. REPORT NUMBER G.L. Report No. 3209
7. AUTHOR(s) Robert L. Byer		8. CONTRACT OR GRANT NUMBER(s) DAAG29-79-C-0181
9. PERFORMING ORGANIZATION NAME AND ADDRESS Edward L. Ginzton Laboratory Stanford University Stanford, CA 94305		10. PROGRAM ELEMENT, PROJECT, TASK AREA & WORK UNIT NUMBERS
11. CONTROLLING OFFICE NAME AND ADDRESS U.S. Army Research Office P.O. Box 12211 Research Triangle Park, NC 27709		12. REPORT DATE November 1980
		13. NUMBER OF PAGES 79
14. MONITORING AGENCY NAME & ADDRESS(if different from Controlling Office)		15. SECURITY CLASS. (of this report) Unclassified
		15a. DECLASSIFICATION/DOWNGRADING SCHEDULE

16. DISTRIBUTION STATEMENT (of this Report)

Approved for public release; distribution unlimited

17. DISTRIBUTION STATEMENT (of the abstract entered in Block 20, if different from Report)

N/A

18. SUPPLEMENTARY NOTES

The view, opinions, and/or findings contained in this report are those of the author(s) and should not be construed as an official Department of the Army position, policy, or decision, unless so designated by other documentation.

19. KEY WORDS (Continue on reverse side if necessary and identify by block number)

Computer-controlled Nd:YAG Pumped $LiNbO_3$ Tunable Source
Radial Birefringent Element
Computer Controlled Laser Attenuator
Slab Configuration Laser Source

20. ABSTRACT (Continue on reverse side if necessary and identify by block number)

We have successfully completed the study, development and application of a computer-controlled Nd:YAG pumped $LiNbO_3$ tunable source. The device has operated reliably for more than one year. It tunes over a 1.4 - 4.0 μm range and operates at resolutions to less than 0.08 cm^{-1} at 10 mJ output at 10 pps.

We have invented and demonstrated a new optical device, the radial birefringent element. We have invented and demonstrated a computer controlled laser attenuator.

.....Continued

DD FORM 1 JAN 73 1473 EDITION OF 1 NOV 65 IS OBSOLETE

UNCLASSIFIED

SECURITY CLASSIFICATION OF THIS PAGE (When Data Entered)

20. (continued)

During the past year we have developed the theory for a slab configuration laser source. We have successfully demonstrated the slab geometry as applied to Nd:Glass. Work is continuing on the understanding and implementation of this high energy, high repetitional rate Nd:Glass slab laser source.

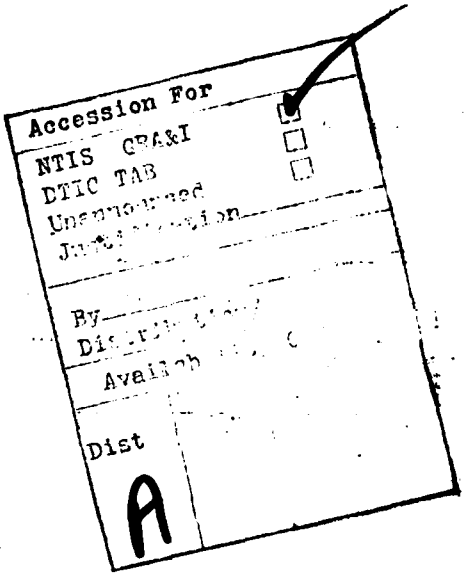

TABLE OF CONTENTS

	Page
Abstract	vi
Forward	1
Tunable Optical Sources	1
A. Statement of the Problem Studied	1
B. Summary of Results	2
C. List of Publications and Technical Reports	4
D. Papers Submitted for Publication	4
E. Participating Scientific Personnel	5
Reprint: "Remote Single-Ended Measurements of Atmospheric Temperature and Humidity at 1.77 μm Using a Continuously Tunable Source," by Endemann and Byer.	6
Reprint: "Computer-Controllable Wedged-Plate Optical Variable Attenuator," by Bennett and Byer	9
Reprint: "Radial Birefringent Element and its Application to Laser Resonator Design," by Giuliani, Park, and Byer	14
Appendix A --"Remote Atmospheric Measurements in the Near Infrared Using a Reliable OPO-Source".	17
Appendix B --"Growth of High Phasematching Temperature $LiNbO_3$ Single Crystals and Application to Efficient Second Harmonic Generation of Nd:YAG"	45

TUNABLE OPTICAL SOURCES

Robert L. Byer
Applied Physics Dept.,
Stanford University

ABSTRACT

We have successfully completed the study, development and application of a computer controlled Nd:YAG pumped $LiNbO_3$ tunable source. The device has operated reliably for more than one year. It tunes over a 1.4 - 4.0 μm range and operates at resolutions to less than 0.08 cm^{-1} at 10 mJ output at 10 pps.

We have invented and demonstrated a new optical device, the radial birefringent element. We have invented and demonstrated a computer controlled laser attenuator.

During the past year we have developed the theory for a slab configuration laser source. We have successfully demonstrated the slab geometry as applied to Nd:Glass. Work is continuing on the understanding and implementation of this high energy, high repetitional rate Nd:Glass slab laser source.

TUNABLE OPTICAL SOURCES

Robert L. Byer

FORWARD

During the past year we have made significant progress in three aspects of tunable laser physics : operation and measurements with a Nd:YAG pumped $LiNbO_3$ Optical Parametric Oscillator Source (OPO);invention, development and demonstration of a new optical element called the Radial Birefringent Element (RBE), and the design and demonstration of a slab configuration Nd:Glass laser oscillator/amplifier system.

We have also invented and developed a computer controlled attenuator and have transferred that technology to industry through the Stanford University License and Technology Office. We have also grown hot phasematching $LiNbO_3$ and have demonstrated efficient second harmonic generation of a cw lamp pumped Nd:YAG laser source.

TUNABLE OPTICAL SOURCES

A. Statement of the Problem Studied

The work during the past year aimed at using nonlinear processes to generate trunable coherent radiation. The work centered on the pump laser sources and improvements in laser source capability. In addition, work progressed on the generation of computer controlled coherent tunable radiation via the Nd:YAG pumped $LiNbO_3$ OPO.

Work began on the study of Nd:Glass as a tunable source. The slab configuration was studied with a design goal of 6 J per pulse at 10 pps tunable output at 1.055 μ ± 100 cm^{-1}. Stimulated Raman shifting is planned for frequency extension to the infrared.

LIST OF APPENDICES

I. M. Endemann and R.L. Byer, "Remote Atmospheric Measurements in the Near Infrared Using a Reliable OPO Source".

II. Y.K. Park, R.L. Byer, R.S. Feigelson and W. Kway, "Growth of High Phasematching Temperature $LiNbO_3$ Single Crystals and Application to Efficient Second Harmonic Generation of Nd:YAG".

B. Summary of Results

During the past year we completed work on the high resolution operation of the computer controlled Nd:YAG pumped $LiNbO_3$ tunable source. We have demonstrated a 4500 cm^{-1} tuning range at 0.6 cm^{-1} resolution; a 0.08 cm^{-1} resolution tunable over a 20 cm^{-1} range; more than one year of operation without optical damage problems, and the capability to make precise atmospheric species, temperature and humidity measurements. The results are summarized in Appendix I and have been presented at recent conferences. M. Endemann's Ph.D. thesis, in preparation, will describe the tunable source in detail. This source was the first computer controlled tunable device.

It now provides the widest tuning range of any tunable source and has operated trouble-free for more than one year. A number of $LiNbO_3$ OPO sources are in operation around the world for remote measurement and laser chemistry research applications. This work is now completed. The four years of research and development have led to a major advance in tunable source science and technology.

Research into methods of improving laser sources continued during the past year. We invented a new optical component, the radial birefringent element, and applied it to laser resonator design. We invented a new computer controlled laser attenuator and demonstrated its capability.

We studied the growth of hot phasematching $LiNbO_3$ for SHG of Nd:YAG. Our work led to the solution a decade old growth problem and to the successful SHG of a Nd:YAG laser at 40% efficiency. This work is summarized in Appendix II.

Our major area of emphasis was the theoretical study of the slab configuration Nd:Glass laser source. We have completed a theoretical description of the slab laser and have developed a first generation numerical program for design calculations. We have designed and constructed a slab glass oscillator. The oscillator verified the theoretical design calculations. It clearly showed the advantages of the slab geometry for glass as well as for high average power Nd:YAG and other crystalline laser materials.

We are actively continuing the experimental and theoretical program on the slab geometry laser approach. We expect to complete

experimental demonstration of the slab glass system in the near future using high quality, optimum finished LHG-5 Hoya glass slabs. This work will then be written as a theoretical/experimental paper on the slab geometry laser approach.

C. List of Publications and Technical Reports

1. M. Endemann and R.L. Byer, "Remote Atmospheric Measurements with a Reliable Tunable OPO Source," Optics Letters, October 1980.

2. K. Bennett and R.L. Byer, "A Computer Controlled Wedged Plate Laser Attenuator," Applied Optics, August 1980.

3. G. Giuliana, Y.K. Park, and R.L. Byer, "Radial Birefringent Element and Its Application to Laser Resonator Design," Optics Letters, November 1980.

D. Papers Submitted for Publication

M. Endemann and R.L. Byer, "Remote Atmospheric Measurements in the Near Infrared Using a Reliable OPO Source."

Y.K. Park, R.L. Byer, R.S. Feigelson, and W. Kway, "Growth of High Phasematching Temperature $LiNbO_3$ Single Crystals and Application to Efficient Second Harmonic Generation of Nd:YAG."

E. Participating Scientific Personnel

Principal Investigator:	Robert L. Byer
Visiting Scholar:	Dr. G. Giuliani University of Rome Italy.
Graduate Student:	Dr. Y.K. Park, Ph.D. earned in the summer of 1980.
Graduate Student:	M. Endemann, Ph.D. expected December, 1980.
Graduate Student:	K. Bennett.

Remote single-ended measurements of atmospheric temperature and humidity at 1.77 μm using a continuously tunable source

M. Endemann and R. L. Byer

Applied Physics Department, Edward L. Ginzton Laboratory, Stanford University, Stanford, California 94305

Received June 9, 1980

Simultaneous remote measurements of temperature and humidity using a narrow-linewidth, continuously tunable, $LiNbO_3$ optical parametric oscillator as a transmitter source are reported. Relative measurement errors of 1.0°C for temperature and better than 1% for humidity over a 45-sec averaging time are observed. The absolute accuracy is limited by the accuracy of available spectroscopic data.

This Letter describes the application of our widely tunable IR air-pollution monitoring system[1,2] to the simultaneous measurement of atmospheric temperature and humidity. Simultaneous remote measurement of these two important meteorological parameters promises to be a useful tool for atmospheric research.

A number of groups have proposed and analyzed methods of making remote temperature measurements, and preliminary remote temperature measurements have been reported using Raman lidar[3] and a two-frequency absorption measurement have been reported.[4] Remote temperature measurements using atmospheric-transmittance measurements of three wavelengths have been analyzed by Mason[5] and by Schwemmer and Wilkerson.[6] Two wavelengths ν_1 and ν_2 are selected to coincide with two absorption lines of one species with different ground-state energy E_i°. A third wavelength ν_{off} is tuned away from the absorption lines and is used to normalize the other two measurements. The absorbance A_i is given by

$$A_i(T) = NL\,\sigma_i(T) = \ln(S_{off}) - \ln(S_i), \qquad (1)$$

where

S_i is the signal received at wavelength ν_i,
N is the density of the species,
L is the pathlength, and
$\sigma_i(T)$ is the absorption cross section at ν_i and temperature T.

The temperature dependence of the absorption cross section is given by the Boltzmann distribution and a partition function $Q(T)$ as

$$\sigma_i(T) = \sigma_i(T_0)Q(T)\exp[(E_i^\circ/k)(1/T_0 - 1/T)] \qquad (2)$$

for an arbitrary reference temperature T_0, where E_i° is the lower-state energy of the transition at ν_i and k is the Boltzmann constant.

From the two measured values $A_i(T)$, we can determine the temperature T as

$$T = \frac{T_0}{1 - \dfrac{kT_0}{E_1^\circ - E_2^\circ}\left[\ln\left(\dfrac{A_1(T)}{A_2(T)}\right) - \ln\dfrac{\sigma_1(T_0)}{\sigma_2(T_0)}\right]} \qquad (3)$$

or, for $(T - T_0)/T_0 \ll 1$,

$$T = C\bar{T} + D, \qquad (4)$$

with $\bar{T} = \ln A_1(T) - \ln A_2(T)$, $C = kT_0^2/(E_1^\circ - E_2^\circ)$, and $D = C[\ln \sigma_2(T_0) - \ln \sigma_1(T_0)] + T_0(k)$.

As expected, the accuracy of the temperature measurement is inversely proportional to the difference in lower-state energies, $E_1^\circ - E_2^\circ$. Once the temperature is known, it is straightforward to calculate the density of the species.

Using selected H_2O transitions permits the simultaneous measurement of temperature and H_2O concentration and thus of relative humidity. Because of the complexity of the spectrum, we used tapes supplied by the U.S. Air Force Cambridge Research Laboratory (AFCRL) to select H_2O lines with appropriate absorption cross-section and ground-state energy differences. For our measurements, the optimum absorption lines were found in the 1.9-μm-band region. The $J = 11$ line at 5651.33 cm^{-1}, with a lower-state energy of 1999 cm^{-1}, and a nearby $J = 6$ line at 5650.41 cm^{-1}, with a 543 cm^{-1} lower-state energy, were selected since their absorption cross sections at room temperature are of similar strength and their absorbance is approximately unity at average H_2O concentrations over a 1-km path. The 1456-cm^{-1} difference in lower-state energy yields a 0.8°C temperature error for a 1% accuracy in determining the absorbance at ν_1 and ν_2.

One problem does arise with this selection of lines. At each wavelength, not only do the selected lines contribute to the measured absorbance; the wings from some strong nearby lines and many weaker, but not negligible, lines also contribute. We used the spectroscopic data contained in AFCRL tapes[7] in a computer program to simulate this interference. Figure 1 shows a simulation of a temperature measurement using the same three wavelengths as were used in the actual experiment. Here $\bar{T}$ [see Eq. (4)] is plotted against the actual temperature T. Overlapping of the two main absorption lines and the influence of other lines and second-order effects make $\bar{T}$ a nonlinear function of T. However, the linear approximation Eq. (4) holds to better than 1° accuracy from −20 to 30°C. Variation of the spectral resolution in the computer simulation shows only small changes of the constants C and D for temperatures above −20°C. Spectroscopic data used

Reprinted from Optics Letters, Vol. 5, page 452, October 1980

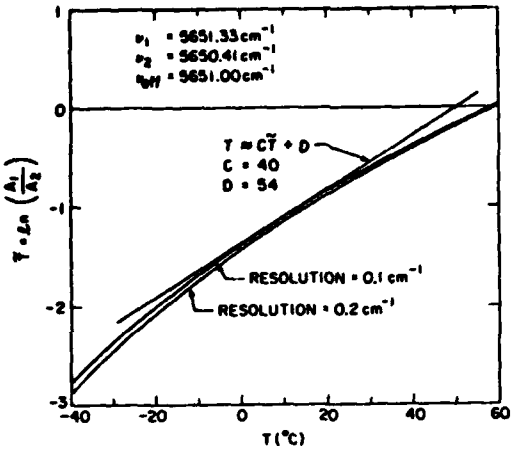

Fig. 1. Temperature calibration using spectroscopic data. For only two absorption lines, the temperature dependence is $T = C\bar{T} + D$. The interference of other lines and the second-order effects of the approximation lead to the slightly curved calibration line. Different probing resolutions change the calibration, but temperature shifts are small above −20°C.

in this simulation have line-strength errors of about 20%, whereas the lower-state energies are known to 0.02 cm^{-1}. The line-strength error affects the constant D, whereas the value for the proportionality constant C is accurate. In actual measurement, we had to use a value for D that is 20°C less than that predicted in the simulation. We are working to improve the spectroscopic data by using our tunable source.

The experimental setup is an improved version of the $LiNbO_3$ optical parametric-oscillator (OPO)-based air-pollution monitoring system.[1,2] An unstable resonator–Nd:YAG laser is used to pump an angle phase-matched $LiNbO_3$ OPO. The OPO is continuously tunable over a 4500-cm^{-1}-wide range, from 1.42 to 4.0 μm. It generates 10-mJ output energy in a 15-nsec-long pulse with a 10-Hz repetition rate. It has operated reliably for more than one year. Details of the tunable source have been reported earlier.[2,8]

The linewidth of the OPO is narrowed to 0.7 cm^{-1} by using an intracavity grating. A tilted étalon further reduces the output linewidth to 0.1 cm^{-1}. This source is continuously tunable by using a PDP11 E10 minicomputer to set crystal angle, grating, and étalon. The OPO output is expanded to a 2.5-cm-diameter beam and directed to the roof of our laboratory, where it is coaxially transmitted through the telescope. The 40-cm-diameter receiving telescope focuses the received light onto a liquid-nitrogen-cooled InSb detector.

Since the output energy of the OPO is not adequate for differential absorption measurements using Mie backscattering, we were limited to long-path absorption measurements using a building at a distance of 775 m as a backscattering target. The height above ground level of this path varies from 10 to 60 m.

A computer was used to tune the OPO and for data taking, averaging, storage, and display. An extensive interactive routine was developed to obtain atmospheric-transmission spectra and to make automatic temperature and humidity measurements. The lower trace in Fig. 2 shows an example of an atmospheric-transmission spectrum with a 0.1-cm resolution tuned over a 17-cm^{-1} range. The upper trace is a simulated transmission spectrum made by using the AFCRL tapes.[7] We used scans similar to this to calibrate the tuning of the OPO and to identify the temperature-sensitive lines.

Once the wavelengths of these lines are determined and the OPO aligned, temperature and humidity measurements are made under computer control. The return signal at each frequency is averaged over several shots before we tune to another line. The time of this average has been optimized to minimize errors that are due to water-vapor fluctuations but to achieve maximum time resolution of the measurement. The OPO is now tuned after 30 shots or 3 sec, which is a good compromise in calm atmospheric conditions. After all three lines are probed, temperature and humidity are calculated, displayed, and stored. Further averaging can be done later; this reduces the storage space required. Also, the standard deviation of each quantity resulting from return-signal fluctuations is determined and stored.

Figure 3 shows the record of temperature and humidity from the morning of March 11, 1980. Each point represents 150 shots/line or averaging over 45 sec. The standard deviation was 1.1°C in the beginning but increased to 1.4°C at 0800 h. The outside weather was cloudy at first, with rain starting at 0740. The rain then increased until it was so strong at 0810 that the measurement had to be interrupted. At 0820 the rain stopped, the cloud cover slowly dissipated, and the wind increased. The remotely measured temperature is compared with a record of a thermograph at the telescope. The general agreement is good. Some discrepancies in the two measurements are expected since the remote measurement averages over a path from 10 to 60 m above the ground and 775 m in length, whereas the thermograph is located on the roof of a building.

The calibration of our data is done by using a large number of remotely measured temperature values (we have accumulated a total of 10 h of data) and comparing

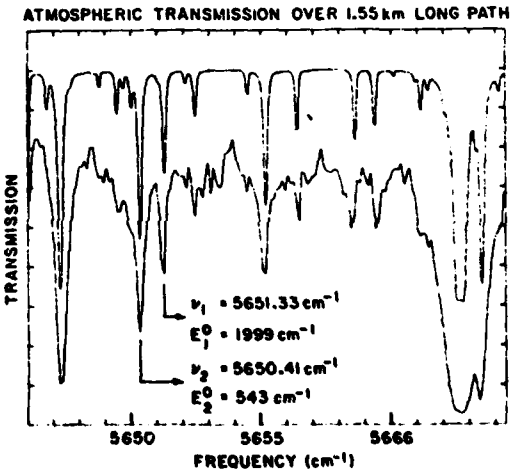

Fig. 2. High-resolution atmospheric scan over 1.55-km path. The OPO linewidth is 0.1 cm^{-1}. The OPO transmission scan (lower trace) is compared with a simulation using AFCRL file data (upper trace).

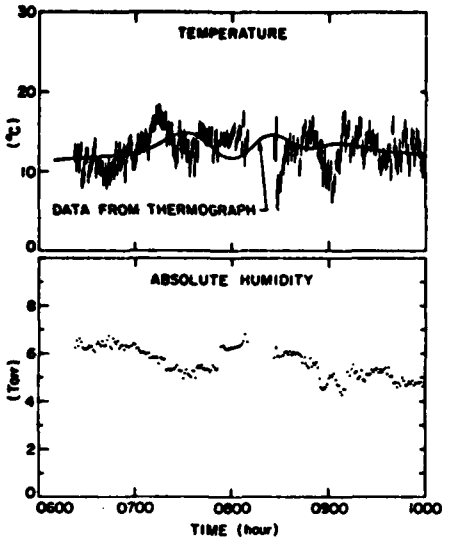

Fig. 3. Temperature and absolute humidity measurement from the morning of March 11, 1980. Temperature data are compared with records from thermograph at receiving telescope.

them with the thermograph data. We found that the best value for the constant D is 35°C, which is 19°C less than the value predicted from the available spectroscopic data.

Our data for humidity measurement have not been checked with an independent instrument so far. We used the absorption strength for the 5650.41-cm^{-1} line from the AFCRL tape,[7] so the accuracy is estimated to be ±20%. We compared our values with relative humidity and temperature measurements at nearby meteorological observation stations. Although the trend of station data confirmed ours, the local fluctuations were too big to improve the calibration for our data.

We have demonstrated the feasibility of measuring temperature and humidity simultaneously by using a high-resolution, continuously tunable source. Absorption lines in the 1.9-μm H_2O band have large enough energy differences in the lower states to permit temperature measurements to be made with 1°C accuracy. Fluctuations of the H_2O concentration do not cause measurement problems as long as the time for each measurement is shorter than the period of these fluctuations.

Our Nd:YAG-pumped, $LiNbO_3$ OPO-based, remote monitoring system proved to be reliable. Operation at narrow linewidth was necessary to resolve the H_2O lines, and the use of a continuously tunable source was essential for optimum line selection. Finally, full computer control was utilized for automatic, long-term remote measurements.

In conclusion, we have measured temperature to 1° accuracy with a time resolution of 45 sec and determined the H_2O concentration with a relative error of less than 1%. However, the absolute accuracy of the humidity data is limited at present by the accuracy of the available spectroscopic data.

We wish to acknowledge the support of the U.S. Army Research Office through contract #DAAG29-77-G-0181 and the Electric Power Research Institute for the continued use of equipment.

References

1. R. A. Baumgartner and R. L. Byer, "Continuously tunable IR lidar with applications to remote measurements of SO_2 and CH_4," Appl. Opt. 17, 3555–3561 (1978).
2. M. Endemann and R. L. Byer, "Remote probing of atmospheric methane over long timescales and high accuracy using widely tunable IR source," presented at the Ninth International Laser Radar Conference, Munich, 1979.
3. A. Cohen, J. S. Cooney, and K. N. Gelleo, "Atmospheric temperature profiles from lidar measurements of rotational Raman and elastic scattering," Appl. Opt. 15, 2896–2901 (1976); see also R. Gill *et al.*, J. Appl. Meteorol. 18, 225 (1979).
4. E. R. Murray, D. D. Powell, and J. E. van der Laan, "Measurement of average atmospheric temperature using CO_2 laser radar," Appl. Opt. 19, 1794–1797 (1980).
5. J. B. Mason, "Lidar measurement of temperature: a new approach," Appl. Opt. 14, 76–78 (1975).
6. G. K. Schwemmer and T. D. Wilkerson, "Lidar temperature profiling: performance simulations of Mason's method," Appl. Opt. 18, 3539–3541 (1979).
7. R. A. McClatchey and J. E. A. Selby, "AFCRL atmospheric absorption line parameter compilation," AFCRL 73-0086 (Air Force Cambridge Research Laboratories, Bedford, Mass., 1973).
8. S. J. Brosnan and R. L. Byer, "Optical parametric oscillator threshold and linewidth studies," IEEE J. Quantum Electron. QE-15, 415–431 (1979).

Reprinted from APPLIED OPTICS, Vol. 19, page 2408 July 15, 1980

Computer-controllable wedged-plate optical variable attenuator

K. Bennett and R. L. Byer

A computer-controllable variable optical attenuator has been developed and tested that has a wide dynamic range, wide spectral range, and is suitable for applications with high peak and average power laser sources. The device is based on Fresnel transmission through two pairs of wedged plates. A 35-dB dynamic range, an insertion loss of 1%, a precision of better than 1% and beam offset and deflection of <0.5 mm and 0.5 mrad, respectively, are demonstrated.

I. Introduction

The ideal optical variable attenuator should provide wide dynamic range, wide spectral range, resettability, and high accuracy, yet exhibit a simple optical and mechanical design. We added the additional requirements that the optical variable attenuator operate with high peak and average power inputs produced by Q-switched laser sources and not significantly alter the beam profile, position, or direction.

With these constraints in mind, we reviewed possible methods of applying the three fundamental interactions that can be used to attenuate optical radiation: absorption; Fresnel reflection at a surface; and interference. Attenuation by absorption and interference were eliminated as not being consistent with the requirements for high peak and average power and wide spectral range.

Fresnel reflection is the basis for many forms of attenuators including those based on birefringent crystals and polarization-dependent total internal reflection.[1] We chose to avoid the use of crystals because of limited spectral range and optical quality. Instead we concentrated on Fresnel reflection near the critical angle in a homogeneous dielectric medium.

The variable gap spacing total internal reflection attenuator[2] is spectrally sensitive and requires tight fabrication tolerances. On the other hand, a variable incident angle wedged-plate attenuator utilizing Fresnel reflection meets all of the above design criteria when properly executed; beam deflection and offset are limited only by fabrication errors.

The theory, design, and performance of the wedged-plate optical attenuator are described in Secs. II–IV.

II. Theory

The power transmittance (T_s) for a single surface depends upon the polarization, the ratio of the indices of refraction n, and the angle of incidence θ_i. The transmittance for light polarized parallel and perpendicular to the plane of incidence is[3]

$$T_{S\perp}(\theta_i,n) = \frac{\sin(2\theta_i)\sin(2\theta_t)}{\sin^2(\theta_i+\theta_t)}, \tag{1}$$

$$T_{S\parallel}(\theta_i,n) = \frac{T_{S\parallel}(\theta_i,n)}{\cos^2(\theta_i-\theta_t)}, \tag{2}$$

where Snell's law in the form

$$n\sin\theta_t = \sin\theta_i \tag{3}$$

applies, and $n = n_t/n_i$ is the index ratio with n_i and n_t the refractive indices of the incident and transmitting media.

Snell's law leads to total internal reflection when no real solution for θ_t exists and occurs only if $n_t < n_i$ or when $n < 1$. To achieve total internal reflection we designed the attenuator to use wedged plates of wedge angle α.

The transmittance of a single wedged plate T_w is the product of the transmittance of two surfaces,

$$T_w(\theta_i,n,\alpha) = T_s(\theta_i,n)T_S(\theta_t+\alpha,\,1/n), \tag{4}$$

and the transmittance of the entire attenuator T is the product of the transmittances of each of the four identical wedges:

The authors are with Stanford University, Edward L. Ginzton Laboratory of Physics, Stanford, California 94305.

Received 2 February 1980.
0003-6935/80/142498-05$00.50/0.

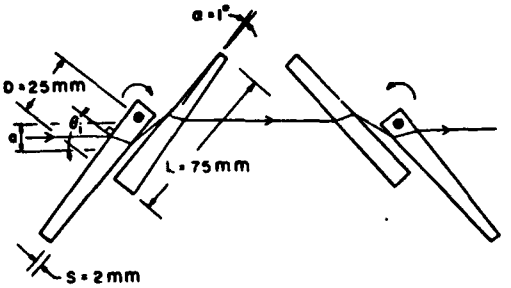

Fig. 1. Schematic of wedged-plate attenuator optical layout. Axes of rotation are shown near base of incident and exit prisms.

$$T = [T_w(\theta_i, n, \alpha)]^4. \tag{5}$$

We define the critical angle of incidence θ_i^{crit} for the wedged plate as the minimum value of θ_i, which results in total internal reflection

$$\sin\theta_i^{crit} = n \sin(u - \alpha); \qquad \text{where } n \sin u \equiv 1. \tag{6}$$

In the next section we apply the above results to the design of a wedged-plate attenuator.

III. Design

A. General Design Procedure

Figure 1 shows the schematic of the wedged-plate attenuator design. The wedge angle α, wedge length L, wedge spacing S, wedge overlap D, and aperture a required to accept the beam are shown. The aperture may be removed from the problem by defining normalized coordinates $l \equiv L/a$, $s \equiv S/a$, and $d \equiv D/a$. The wedge length L' must be sufficiently longer than L to account for wedge thickness and fabrication. To design the attenuator the four parameters α, l, s, and d must be chosen. The primary considerations are the maximum attenuation required and the allowable interference. For large aperture ratios ($l \geq 15$), nonuniformity of the attenuation arising from beam divergence may be a consideration at extremely high attenuations. Insertion loss for the polarization in the plane of incidence is <1% for $l > 4$ and $n \approx 1.5$ and is relatively independent of the wedge angle for the orthogonal polarization.

The fractional beam expansion in the plane of incidence is given by

$$\frac{\Delta a}{a} \approx 2 \frac{\cos^2\theta_i}{\cos^3\theta_{t_2}} \Delta\theta_i, \tag{7}$$

$$\sin\theta_{t_2} = n \sin(\alpha + v), \tag{8a}$$

$$n \sin v = \sin\theta_i, \tag{8b}$$

where θ_{t_2} is the angle between the normal to the wedge and the beam in the gap between wedges in a pair, and $\Delta\theta_i$ is the full angle of the incident laser beam divergence (radians). The beam expansion $\Delta a/a$ is $<200\Delta\theta_i$ for the designs considered here and is not an important consideration.

The wedge angle α is chosen so that the laser beam is entirely intercepted at the critical angle given by Eq. (6). The wedge angle is

$$\alpha = u - w, \tag{9a}$$

where

$$\sin w = 1/n \sin(\text{arcsec } l). \tag{9b}$$

The wedge spacing s is determined from the maximum allowable interference. Interference occurs when beams multiply reflected by the parallel surfaces on either side of the gap are not offset by at least the aperture a. Assuming a uniform intensity across the aperture and zero elsewhere, the fraction I of the transmission through the aperture, which is doubly reflected, is

$$I = r^2(\theta_{t_2})(1 - 2s \tan\theta_{t_2} \cos\theta_i) \tag{10}$$

if $2s \tan\theta_{t_2} \cos\theta_i < 1$ and is zero otherwise. Here $r = 1 - T_s(\theta_{t_2}, n)$.

After choosing a maximum value of I for each polarization, the required wedge spacing is found by numerically solving for the maximum value of s as a function of θ_{t_2}. For the polarization in the plane of incidence, s has a single maximum for θ_{t_2} greater than Brewster's angle.

A minimum wedge overlap d is required in each wedged-plate pair to avoid beam clipping by the second wedge. Snell's law and geometry yield

$$d = 1/\cos\theta_i - s \tan\theta_{t_2} \tag{11}$$

for the beam walk where the thickness of the optics has been neglected. This function has a single maximum in the domain of interest and is again computed numerically using the value of s determined above.

The maximum attenuation is limited by clipping of the outside edge of the second wedge. This occurs for

$$\tan\theta_{i_2} \geq [(l - d)/s]. \quad (12)$$

The maximum attenuation is found by applying Eq. (5) with θ_i calculated from Eqs. (8a) and (8b).

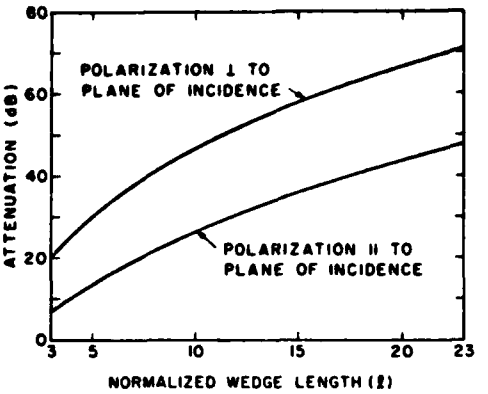

Fig. 2. Maximum attenuation vs aperture ratio l for $n = 1.45$, 1.0% maximum interference in Brewster polarization (see text).

B. Numerical Design

Figures 2 and 3 can be used to design attenuator optics. These were computed assuming $n = 1.45$ and a 1% maximum interference in the Brewster polarization, which implies a 3–6% maximum interference in the orthogonal polarization. The procedure is as follows:

(1) Determine the desired maximum attenuation and find the required normalized length from Fig. 2, which was calculated according to the method of the previous section, specifically Eqs. (5) and (9)–(12). The wedge length must be la + wedge thickness + fabrication tolerance.

(2) Determine the wedge angle α from Eq. (9). This is shown along the top axis of Fig. 3.

(3) Read off the spacing and overlap requirements from Fig. 3.

Interference can be reduced by increasing the spacing. However, an increase in wedge spacing also reduces the maximum attenuation.

Using these equations and design procedure, we evaluated the attenuator performance as a function of wedge angle and index of refraction for a number of factors of interest including attenuator dynamic range, insertion loss, beam displacement and angular deviation, and acceptance angle. One design that provided a good compromise between attenuation range and ease of optical and mechanical fabrication is described next.

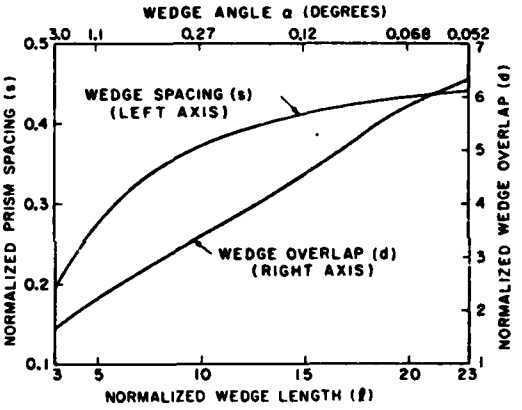

Fig. 3. Normalized wedge spacing s, normalized wedge overlap d, and wedge angle α for the specifications of Fig. 2.

C. Specific Wedged-Plate Attenuator Design

Figure 1 shows a schematic of the wedged-plate attenuator. Four identical uncoated fused silica wedges were fabricated with $\lambda/10$ quality surfaces and wedge angles $\alpha = 1°$. This design is not strictly according to the criteria of the above section, because the attenuator was designed to work well both for a 1-mm diam, 1-mrad divergence beam and 6-mm diam, 0.5-mrad divergence beams with a 10-mm positioning aperture. The pairs of wedges were mounted on counterrotating shafts located to minimize beam displacement and optical alignment problems. The shafts were driven by independent stepper motors geared through antibacklash worm gears to a ratio of 2400 steps/rad.

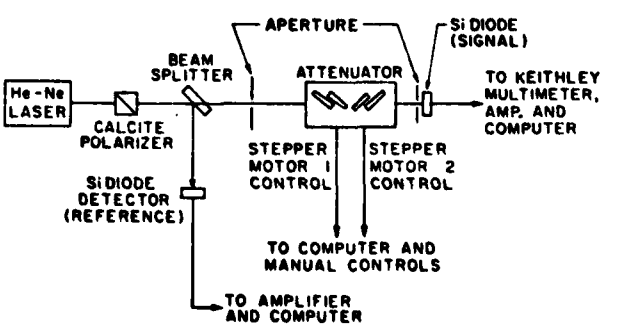

Fig. 4. Schematic of optical and electrical system used for attenuator calibration measurements.

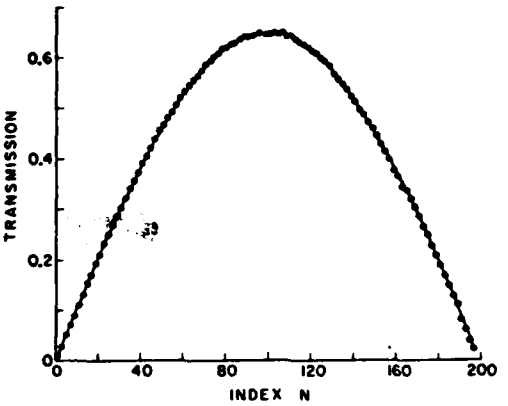

Fig. 5. Measured transmittance $T_N = 0.6 \sin(N\pi/200)$ vs stepper motor position N: ●, data points; —, theoretical transmittance; rms error is 0.008.

The wedges were fabricated 75 mm in length. Alignment of the wedges within a pair must be within the diffraction angle of the incident beam to avoid significant beam deflection. The wedges do induce some beam expansion in the plane of incidence. However, for incident light polarized perpendicular to the plane of incidence, beam expansion is <0.5 mm for a 1-mrad divergence input beam at the 38-dB attenuation level and decreases rapidly at lower attenuations. The calculated insertion loss is 24% for a dynamic range of 35 dB in this polarization.

For a beam polarized parallel to the plane of incidence and incident at Brewster's angle, the calculated insertion loss of the attenuator is <0.1%. The attenuator provides 15-dB dynamic range in this polarization.

IV. Measurement Results

The performance of the attenuator was verified using a polarized He–Ne laser source and a wide dynamic range silicon diode detector. The attenuator was controlled by a PDP11/10 minicomputer that set the stepper motors and recorded the transmitted and reference powers at 1-sec intervals for each stepper motor position. A schematic of the experimental setup is shown in Fig. 4.

The attenuator was placed in the He–Ne beam path in approximate alignment. Final angular alignment of the prisms was accomplished to within 0.5 mrad by manually stepping the motors to critical angle independently. This procedure provided an absolute orientation for the prisms and proved to be very repeatable.

The laser output was then blocked, and the dark current was measured for the signal and reference channels. These levels were used as the zero signal levels for the subsequent measurements.

To show the versatility and the dynamic range of the attenuator, two driving patterns were chosen. The first in a sine attenuation curve, and the second is a scan at constant angular rate. The sine attenuation routine calculates the proper number of motor steps to generate a power transmittance function $T_N = 0.6 \sin(N\pi/200)$ accurate to ±0.0025. The data obtained by this routine are shown in Fig. 5 for polarization perpendicular to the plane of incidence. The theoretical curve, which is drawn as a solid line in Fig. 5, is calculated according to the actual motor setting and scaled to account for a measured 1% scatter loss. The average rms error between the actual and calculated attenuation is

$$\epsilon = \left[\sum_i \frac{(x_i^{\text{exp}} - x_i^{\text{theory}})^2}{n-1}\right]^{1/2} = 0.008.$$

The error agrees well with the average standard deviation of the data of 0.01 and the expected average digitization uncertainty of 0.005.

Figure 6 shows the attenuation obtained for polarization perpendicular to the plane of incidence as a function of scan angle relative to the critical angle. For the fused silica wedges used, $n = 1.45$ and $\theta_i^{\text{crit}} = 79.0°$ for $\alpha = 1°$. The attenuation is plotted on a semilog scale to illustrate the wide dynamic range. To retain signal levels for accurate digitization, the amplifier gain settings were changed and normalization chosen for each setting to match the data points in overlapping regions. The maximum attenuation was ~4000:1, and the insertion loss for this polarization was 25%, which yields a dynamic range of 35 dB. The average rms error ϵ was 7, 1.5, 2, and 0.7% for the >30-, 20–30-, 10–20-, and 10-dB attenuation ranges. The error is larger in the 10–20-dB range, because the amplified signal was smaller, which led to increased electrical noise and digitization errors. Data in the 15–20-dB range were taken at a higher amplifier gain setting and had an rms error of 1%. All averages are within one standard deviation of the theoretical values.

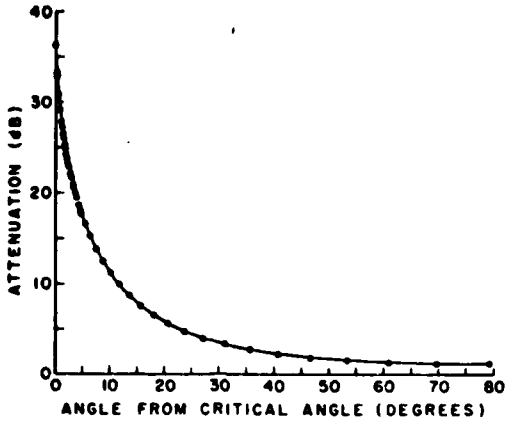

Fig. 6. Attenuation in dB vs angle from critical angle for incident He–Ne beam polarized perpendicular to the plane of incidence: ●, measured data points; —, theoretical attenuation.

In addition, all points in the >30-dB range showed a transmittance in excess of the theoretical value. This is due to some residual component of the orthogonal polarization. For example, an orthogonal polarization component of only one part in seven hundred would account for the 7% extra transmittance in the >30-dB range.

Similar data were taken for the Brewster polarization, and a maximum attenuation of 15 dB was measured as expected. The measured insertion loss was near 1%, which is significantly greater than the expected 0.1% loss. However, eight wedge surfaces provide ample opportunity for scatter losses to contribute to the attenuation.

The attenuator performance was also verified with a Q-switched Nd:YAG laser source operating at 70 mJ/pulse in a 6-mm diam beam. Since only uncoated fused silica surfaces are employed, the attenuator should operate at incident energy densities limited only by the surface damage threshold of fused silica >3 J/cm^2.

V. Conclusion

We developed a simple but versatile computer-controllable optical variable attenuator suitable for use with virtually all collimated light sources, including high power Q-switched lasers. The spectral response is extremely flat and can be accurately calculated from the refractive index. The useful spectral range is very broad limited only by the transmittance range of the wedge material. The optical fabrication and mechanical design are straightforward, and the attenuator does not require dielectric or metallic coatings. Fresnel's equations and a knowledge of the wedged-plate indices of refraction lead to an absolute value of attenuation with an accuracy limited by the knowledge of incident polarization. Transmittances precise to <2% are easily obtained. Absolute accuracy can be improved by using two attenuators in tandem with relative planes of incidence rotated by precisely 90° to eliminate polarization dependence.

The attenuation has a scatter-limited insertion loss for the Brewster polarization of <1% and a dynamic range of 15 dB. The non-Brewster polarization insertion loss is 25% with a dynamic range of 35 dB. Beam deflection and offset are limited by fabrication and optical alignment tolerances. A simple hand assembly technique resulted in negligible beam offset and deflection except at the highest attenuation levels where the measured offset is <0.5 mm and deviation <0.5 mrad at attenuations >35 dB.

We designed the attenuator to meet a number of cw and pulsed laser attenuation requirements in our laboratory. We expect that the wedged-plate attenuator has many uses, including nonlinear optical studies, detector linearity and calibration measurements, absolute phototube calibration, tunable laser intensity control, and in absorption spectroscopy as part of a null detector servo system.

We would like to thank George Kolter for fabricating the optics, Martin Endemann for his assistance with the computer, and S. Byer for data tabulation.

This work was supported by the Air Force Office of Scientific Research under contract AF49620-77-C-0092 and by the Army Research Office under contract DAAG29-77-G-0221.

References

1. F. A. Jenkins and H. E. White, *Fundamentals of Optics* (McGraw-Hill, New York, 1957).
2. T. Oshi and S. Saito, Appl. Opt. **10**, 144 (1971).
3. M. Born and E. Wolf, *Principles of Optics* (Macmillan, New York, 1975), p. 42.

Radial birefringent element and its application to laser resonator design

G. Giuliani,* Y. K. Park,† and R. L. Byer

Edward L. Ginzton Laboratory, Applied Physics Department, Stanford University, Stanford, California 94305

Received July 18, 1980

We have invented a quasi-Gaussian profile-transmittance filter based on radially varying the phase retardation in a birefringent element. The radial birefringent element has been applied to resonator design and has demonstrated its usefulness in generating an improved resonator spatial-mode profile.

It has been known for more than one decade that resonators constructed with a Gaussian profile-reflector element offer the possibility of arbitrary large mode diameters,[1-4] thus overcoming the small-mode-volume limitation of TEM_{00} mode resonators. To date, experimental verification of the theory has not been demonstrated. It has also been recognized that unstable resonators[5] offer an advantage of large mode volume, but at a sacrifice of mode quality because of aperture-generated Fresnel fringes.[6,7] Furthermore, the stability of unstable resonators improves with increasing magnification and thus with higher output coupling. Thus unstable resonators have been limited to relatively high-gain laser media, such as CO_2 (Ref. 8) and Nd:YAG.[9]

We propose an elegant yet simple optical device, the radial birefringent element (RBE), as a method of realizing a Gaussian reflectance profile. We show that the RBE can be used in both stable and unstable resonators to realize the advantages predicted by theory. In particular, the RBE, in conjunction with an unstable resonator, provides a smooth spatial-mode profile and arbitrary output coupling and yet maintains the stability associated with large-magnification unstable resonators.

The RBE is shown schematically in Fig. 1 as the end reflector of a resonator. The element consists of a birefringent crystal with a radius of curvature polished on one surface situated between a polarizer and an end mirror. The reflectance at the center of the element is determined by the net phase retardation $\phi_0 = 2\pi\Delta n l_0/\lambda$, where Δn is the birefringence, l_0 is the physical thickness, and λ is the wavelength. Since the phase retardation $\phi(r)$ is a function of radial position, the reflectance also varies radially. If we assume that the reflected beam retraces the optical path of the forward beam at the element, an analysis of the mirror, polarizer, and RBE combination using Jones's matrix approach[10] shows that the reflectance and transmittance of the device are given by

$$R = \cos^2\phi(r) + \sin^2\phi(r)\cos^2 2\theta, \tag{1a}$$

$$T = \sin^2\phi(r)\sin^2 2\theta, \tag{1b}$$

where θ is the angle between the polarizer and the principal axis of the birefringent plate. To a good approximation,

$$\phi(r) = \frac{2\pi\Delta n}{\lambda} l(r) = \frac{2\pi\Delta n}{\lambda}\left(l_0 \pm \frac{r^2}{2\rho}\right), \tag{2}$$

where r is the radial position and ρ is the curvature, with the upper and lower signs corresponding to convex or concave curvatures, respectively. Equation (1a) can be written in the form

$$R(r) = \cos^2 2\theta + \sin^2 2\theta \cos^2\phi(r),$$

which explicitly shows that the reflectance is given by a constant factor depending on θ modulated by a term varying as $\cos^2\phi(r)$ with amplitude $\sin^2 2\theta$. For $\theta = 45°$, we find that $R(r) = \cos^2\phi(r)$, or

$$R(r) = \cos^2\left[\frac{2\pi\Delta n}{\lambda}\left(l_0 \pm \frac{r^2}{2\rho}\right)\right]. \tag{3}$$

If we want to set $R(r) = 0$ at a specific radius r_0, determined, for example, by an aperture or rod radius within the resonator, then Eq. (3) can be inverted to give

$$l_0 = \frac{\lambda}{2\pi\Delta n}\{\cos^{-1}[R(0)]^{1/2} + m\pi\},$$

$$\rho = \frac{r_0^2\Delta n 2\pi}{2\lambda}\{\cos^{-1}[R(r_0)]^{1/2} - \cos^{-1}[R(0)]^{1/2}\}^{-1}, \tag{4}$$

where m is an integer.

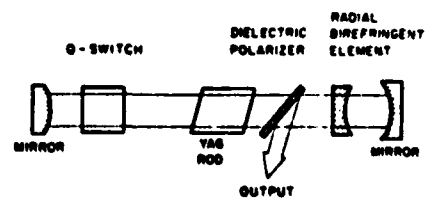

Fig. 1. The radial birefringent element consisting of a polarizer and a birefringent plate with curvature ρ, within an unstable resonator cavity.

0146-9592/80/110491-03$0.50/00

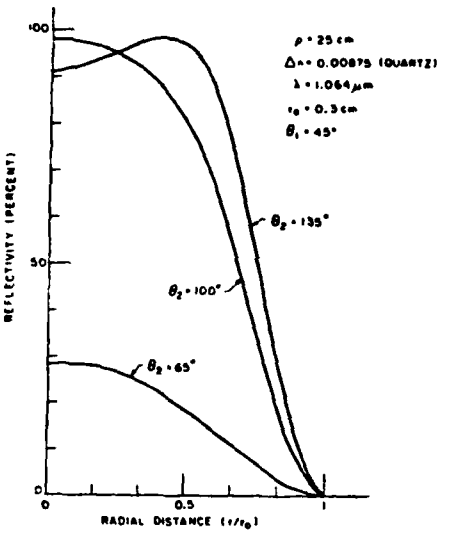

Fig. 2. Reflectance profiles of the RBE using two crystal-quartz elements. Two elements have equal but opposite curvature ρ. θ_1 and θ_2 are the angles between the principal axis of the quartz elements and the polarizer axis. The mode radius r_0 is chosen equal to the radius of the Nd:YAG rod.

It is convenient to define the equivalent Gaussian spot size of the RBE w_m as

$$w_m{}^2 = r_0{}^2 \frac{\cos^{-1}[R(0)/e]^{1/2} - \cos^{-1}[R(0)]^{1/2}}{\cos^{-1}[R(r_0)]^{1/2} - \cos^{-1}[R(0)]^{1/2}}, \quad (5)$$

where e is the Neper number. Note that for $R(0) = 1$ and $R(r_0) = 0$, $w_m{}^2 = 0.58\, w_0{}^2$, and that, unlike for a Gaussian reflector, we can arrange $R(r_0) > R(0)$. Thus the RBE is a pseudo-Gaussian mirror with reflectance

$$\sqrt{R(0)}e^{-(r^2/w_m{}^2)}.$$

Equation (5) can be used with previous analyses of resonators[1] with Gaussian reflectance elements as the effective spot size of the Gaussian reflector.

Finally, for ABCD resonator analysis of the cavity shown in Fig. 1, the radius of curvature of the equivalent mirror is given by

$$R_e = \left(\frac{1}{R_m} + \frac{1}{f}\right)^{-1}, \quad (6)$$

where f is the focal length of the birefringent plate with curvature ρ and R_m is the end mirror's radius of curvature. This is a good approximation when the element is a distance from the end mirror that is small compared with the mirror's curvature or the element's focal length.

We have also designed, constructed, and analyzed[11] other variations of the RBE. Of interest for resonator studies is a two-element RBE consisting of a positive-curvature element next to a negative-curvature element. By varying the angles θ_1 and θ_2, which are the angles between the polarizer and the principal axis of the birefringent elements, various reflectance profiles can be generated. Figures 2 shows some reflectance profiles for various θ_2 and fixed θ_1. Here both elements have equal refractive indices and equal but opposite curvatures ρ. This variation of the RBE was used in the resonator studies described next.

We have constructed both stable and unstable resonators using the RBE for a Nd:YAG gain medium. The resonators with the geometric magnification larger than 2 demonstrated that large TEM_{00} mode spot sizes could be supported, as expected from previous theoretical analysis.[1,3,4] However, when the mode size is big enough to extract high energy from the rod, the diffraction loss that is due to the rod causes the stability of such a resonator to be marginal.

The RBE in combination with an unstable resonator offers the advantages of good alignment stability, excellent output spatial-mode profile, and good discrimination against higher-order modes. The RBE was constructed by combining a convex and a concave crystal quartz lens with equal ρ = 25-cm curvatures. The mirror curvatures of the RBE resonator were chosen to form an unstable resonator with the thermal focusing of the rod taken into account. Best collimation at the output was achieved with the combination of a −400-cm-curvature mirror and a −200-cm-curvature mirror. The resonator length was 65 cm. In this resonator, the output coupling was changed by rotating the RBE. The optimum performance was found when θ_1 = 45° and θ_2 = 100°, although the angles were relatively uncritical with $\Delta\theta_1 = \pm 5°$ and $\Delta\theta_2 = \pm 10°$.

We chose to compare the RBE resonator performance against the standard 60-cm-long, M = 3.3 Nd:YAG confocal unstable resonator.[9] Figure 3 shows the transverse-mode quality of the RBE unstable resonator and the confocal unstable resonator with a 1.8-mm-diameter polka-dot-coated output coupler. The video scans clearly show the flat-top profile of the RBE resonator compared with strongly Fresnel-modulated unstable-resonator output.[7] The RBE, with its $\cos^2 \phi(r)$ reflectance profile, effectively eliminates

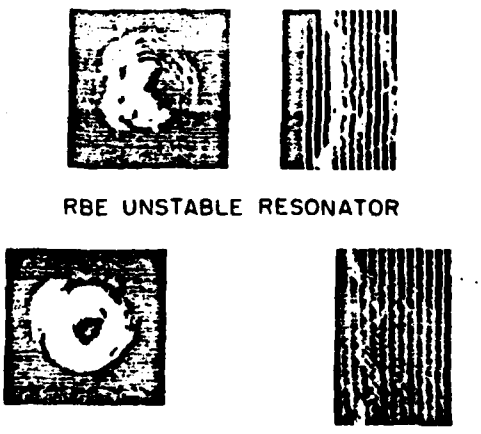

Fig. 3. Transverse-mode profiles of the RBE and standard confocal unstable resonator configurations. The Polaroid exposures of the output are at the right side and the vidicon-scanned profiles are at the left side. The slightly asymmetric patterns are due to a damage spot on one end of the Nd:YAG rod.

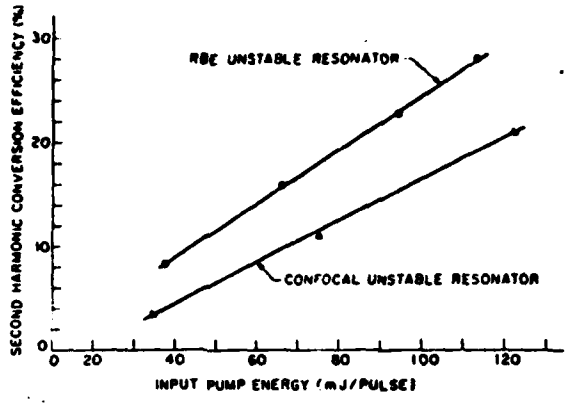

Fig. 4. Second-harmonic-generation conversion efficiency versus input pump energy for the confocal unstable resonator and for the RBE unstable resonator in Type II KD*P.

Fresnel fringes that arise from diffraction caused by hard apertures. The weak Fresnel fringes on the profile of the RBE resonator are due to the finite aperture size of the YAG rod.

As a further comparison of performance, we carried out second-harmonic-generation (SHG) conversion-efficiency measurements in a Type II angle-phase-matched KD*P crystal. Figure 4 shows the improved SHG performance of the RBE unstable resonator.

In conclusion, we have invented a new class of optical elements based on radially varying the phase retardation in a birefringent plate. In particular, the radial birefringent element has been applied to resonator design and has demonstrated its usefulness in generating an improved resonator spatial-mode profile and improved nonlinear conversion. The RBE is simple to implement and should prove useful in designing unstable resonators for large-aperture but low-gain laser media. The RBE should also find applications as a spatial filter or soft aperture.

We wish to acknowledge the support provided by the U.S. Air Force Office of Scientific Research under grant #AFOSR-80-0144 and the support provided one of us by the NATO Fellowship Program.

* Visiting scholar from the University of Rome, Italy.

† Present address, System & Research Center, Honeywell, Minneapolis, Minnesota.

References

1. L. W. Casperson, "Mode stability of lasers and periodic optical systems," IEEE J. Quantum Electron. QE-10, 629–634 (1974).
2. L. W. Casperson and S. D. Lunnam, "Gaussian modes in high loss laser resonators," Appl. Opt. 14, 1193–1199 (1975).
3. U. Ganiel and Y. Silberberg, "Stability of optical resonators with an active medium," Appl. Opt. 14, 306–309 (1975).
4. A. Yariv and R. Yeh, "Confinement and stability in optical resonators employing mirrors with Gaussian reflectivity tapers," Opt. Commun. 13, 370–374 (1975).
5. A. E. Siegman, "Unstable optical resonators for laser applications," Proc. IEEE 53, 217–287 (1965); "Unstable optical resonators," Appl. Opt. 13, 353–367 (1974).
6. A. J. Campillo *et al.*, "Fresnel diffraction effects in the design of high power laser systems," Appl. Phys. Lett. 23, 85–87 (1973).
7. S. Sheng, "Studies of laser resonators and beam propagation using fast transform methods," Ph.D. thesis, Ginzton Laboratory Report #3106 (Stanford U. Press, Stanford, Calif., 1979).
8. W. F. Krupke and W. R. Sooy, "Properties of an unstable confocal resonator CO_2 laser system," IEEE J. Quantum Electron. QE-5, 575–586 (1969).
9. R. L. Herbst, H. Komine, and R. L. Byer, "A 200 mJ unstable resonator Nd:YAG oscillator," Opt. Commun. 21, 5–9 (1977).
10. R. C. Jones, "A new calculus for the treatment of optical systems," J. Opt. Soc. Am. 32, 486–493 (1942).
11. G. Giuliani and R. L. Byer, "The radial birefringent element" (to be published).

APPENDIX A

Edward L. Ginzton Laboratories of Physics
Stanford University
Stanford, Ca 94305

REMOTE ATMOSPHERIC MEASUREMENTS IN THE NEAR INFRARED USING A RELIABLE OPO-SOURCE

M. Endemann, R.L.Byer
Applied Physics Departement
Stanford University

October 2, 1980

REMOTE ATMOSPHERIC MEASUREMENTS IN THE NEAR INFRARED USING A RELIABLE OPO-SOURCE

M.Endemann, R.L.Byer
Applied Physics Departement
Stanford University

ABSTRACT

A reliable single ended remote monitoring LIDAR operating in the infrared is described. The system uses a 1.4 to 4.0 µm tunable OPO source as transmitter. Continuous remote monitoring of atmospheric methane over a 17 hour period demonstrates the reliability of the system. Simultaneous remote measurements of temperature and humidity using absorption lines of the 1.9 µm water band achieve relative accuracies of 1.0°C and 1 % respectively over a 45 sec. averaging period. The expected sensitivity for the measurement of other pollutants with absorption lines within the tuning range of the transmitter is discussed.

I. INTRODUCTION

The need for single ended air pollution monitoring systems is now well established and the methodology of making remote measurements is understood[1]. The monitoring of industrial pollution and the measurement of trace constituents are efficiently done using a single-ended remote probing technique. Furthermore, remote probing is evolving into an important research tool for studying transport, mixing and chemistry of trace constituents in the atmosphere. Recent experiments have also shown the potential for simultaneous remote humidity and temperature measurements for metereology.

In their review article Kildal and Byer[2] found that remote measurements using absorption promised the highest sensitivity and lowest required powerlevels. In a later paper, Byer and Garbuny[3] analyzed remote measurement methods including single ended absorption with topographic targets and depthresolved absorption using Mie scattering as a distributed retroreflector. For long path absorption a narrow bandwidth laser beam is transmitted through the atmosphere to a distant topographic target. Some portion ρ of this beam is scattered back by the non cooperative target, and is collected by a telescope at the transmitter end. The received energy $S(\nu)$ is determined by using conservation of energy leading to the LIDAR-equation

$$S(\nu)=E_0(\nu)\eta A/R^2\rho * e^{-2\int_0^R\{\alpha_{sca}(r)+N(r)\sigma(\nu)\}dr} \qquad [1]$$

where

- E_0=transmitted light-energy of frequency ν
- η=efficiency of optical system
- A=area of receiving telescope
- R=distance to backscattering target
- $\rho(R)$=backscattering due to target at distance R
- α_{sca}=attenuation coefficient due to atmospheric scattering-losses
- N(r)=numberdensity of species to be probed
- $\sigma(\nu)$=absorption cross section of species at wavelength ν

In the near infrared, topographic targets scatter 1 to 10 % of the incident light back toward the receiving telescope. The average concentration of a pollutant along the lightpath $N \equiv \int N(r)dr/R$ is measured by transmitting two pulses with different frequencies ν. If the frequency change is small, only the absorption cross section of the pollutant changes, so that the concentration N derived from (1) is

$$N = \frac{\ln\{S(\nu_1)/S(\nu_2)\}}{2R\{\sigma(\nu_2)-\sigma(\nu_1)\}} \qquad [2]$$

where the absorption cross sections $\sigma(\nu_i)$ have been previously determined. Fixed frequency lasers have only a few coincidences with absorption lines of interest[4] so that for most applications a tunable laser is preferred.

From 1974 on many remote monitoring systems have been developed and tested using tunable dye lasers[5/6]. Initially the reliability of many of these systems was marginal, but recently a number of systems with excellent reliability using commercially available Nd:Yag pumped dye lasers have been reported[7/8]. A series of field measurements have demonstrated the usefulness of remote pollution detection[8]. However, dye laser measurements in the visible and ultra-violet region is limited to the measurement of only three pollutants: SO_2, NO_2, and O_3.

To extend the LIDAR measurements to other atmospheric constituents, the infrared spectral region must be used. Line tunable CO_2, recently doubled CO_2 and DF lasers have been used[9/10/11], but are limited to spectral coincidences with absorption lines of pollutant molecules. To achieve wider pollutant selection and better measurement sensitivity, we have developed a continuously tunable high power infrared source which is used as transmitter for a single ended remote measurement system. The transmitter is an Optical Parametric Oscillator (OPO), which is continuously tunable from 1.4 to 4.0 µm. Initial measurements of SO_2[12] and also CH_4[13] with this system have been reported by Baumgartner and Byer. Improvements in the design of the OPO transmitter which increased the reliability and spectral resolution considerably were described by Brosnan and Byer[14]. Increased output energy up to 70 mJ per pulse at 10 Hz was achieved with an Optical Parametric Amplifier (OPA) discussed by Baumgartner and Byer[15]. Extensive software develoepement has enabled automatic pollution measurements to be made over timescales of many hours as demonstrated by recent CH_4 measurements[16].

II. SYSTEM DESCRIPTION

The Stanford LIDAR transmitter is an angle phasematched, singly resonant $LiNbO_3$ Optical Parametric Oscillator (OPO). For the methane measurements the OPO was amplified by an Optical Parametric Amplifier (OPA). OPO and OPA are described in detail by Brosnan and Byer[14] and Baumgartner and Byer[15].

Fig.1 shows a diagram of the transmitter. The Q-switched unstable resonator Nd:Yag laser generates 220 mJ energy per pulse with a 10 Hz repetition rate. The length of the resonator is 1.40 m to generate 18 nsec long Q-switched pulses. This pulselength is ideal to pump the OPO, since the optical intensity of the pumpbeam is low enough to avoid damage of the $LiNbO_3$ crystal due to self focusing, but the oscillation threshold of the OPO still is low due to decreasing build-up losses[14].

The output of the Nd:Yag laser is slightly demagnified to a 5 mm diameter beam and directed into a folded 15 m long path. This distance is adequate, to transform the unstable resonator 1.06 µm beam into the far field Airy-disk mode with 60% of the beam energy in the central lobe. Oscillation threshold of the OPO is considerably decreased with

this pump beam compared to pumping with the near field unstable mode. The danger of surface damage to the $LiNbO_3$ crystal is also removed. The pointing stability of the long-cavity Nd:Yag laser and the far field converter is critical for the reliabitlity of the system. We used fused silica rods to stabilize the Nd:Yag resonator structure, and mounted the steering mirrors for the folded 15 m path length far field converter directly onto the laser resonator structure. This arrangement gives excellent pointing stablilty of the beam.

For operation of the OPA 40% of the 130 mJ of 1.06 μm energy is split off into a Nd:Yag amplifier, while the mainpart is directed through a 2.2X demagnifying telescope to pump the OPO. The OPO uses a 50 mm long, 20 mm diameter $LiNbO_3$ crystal to generate the signal and idler output. The signal wave tunes from 2.1 to 1.4 μm, while the idler wave tunes from 2.1 to 4.0 μm for a 4^0 change in the $LiNbO_3$ phase matching angle. The tuning range is limited by absorption of the idler wave in the $LiNbO_3$ crystal at 4 μm. The OPO uses an L-shaped resonator which reflects only the signal wave. The resonator uses a flat outputcoupler with 50% reflectivity between 1.4 and 2.1 μm, and a 600 gr/mm grating. In order to improve the resolution of the grating, a 10:1 ZnSe prism beam expander[17] is inserted into the cavity. With grating and prism beam expander the linewidth at half intensity points is less than 0.8 cm^{-1} for the signal wave. To improve the resolution further, a tilted etalon can be inserted into the cavity. For a 2 mm thick etalon the signal output linewidth is less than 0.1 cm^{-1}. The linewidth of the idler output is about equal to the sum of the widths of signal and pump beam. The Nd:Yag laser has a linewidth of 0.4 cm^{-1}, but can easily be reduced to 0.01 cm^{-1} by inserting a tilted etalon.

Output energy of the OPO is 5 mJ in the signal wave over most of the tuning range. Due to the absorption losses of the idler wave in the $LiNbO_3$ crystal, the threshold increases near the end of the tuning range and the output energy decreases. The energy of the idler output is equal to the energy in the signal wave multiplied by the ratio of the photon energies.

Astigmatic beam divergence was observed in the OPO output beams when the grating-prism beam expander is used for linewidth control. With the etalon the output beam has a symmetrical divergence and can be collimated.

The OPA consists of a Nd:Yag pumped 50mm x 20 mm angle phasematched $LiNbO_3$ crystal. It increases the output energy from the OPO to more than 12 mJ in the signal wave. However, for the temperature and humidity measurements only the OPO was used. This simplified the set up, and yet provided enough energy to see a strong backscattering signal from topographic targets. Table 1 summarizes the transmitter parameters for the different measurements.

About 1% of the tunable light energy is used for diagnostic purposes. The lack of wavelength resettability of the OPO in early experiments led to the introduction of a photo-acoustic cell to monitor the proper tuning of the OPO by observing the absorption cross section during an extended measurement. Improvements of the tuning mechanism made continuous monitoring of the cross section superfluous and later the cell was used only for spectroscopic measurements. An InSb detector is used as reference detector to ratio out energy fluctuations of the OPO/OPA. An absorption cell follows to determine the absorption cross section of a pollutant at a given wavelength.

The main portion of the beam is expanded in a 10:1 telescope to about 2.5 cm diameter and transmitted coaxially from the receiving telescope on the roof of our laboratory. This receiving tele-

scope is a 40 cm diameter, f=3 Newtonian design. It collects and focuses the backscattered light onto a liquid nitrogen cooled InSb detector.

Fig.2 shows a diagram of the electronics. The amplified signal and reference pulses are integrated and digitized for the computer, which ratios and averages the signals. The signal from the photoacoustic cell is amplified in a Lock-in amplifier, which is tuned to the resonance frequency of the cell and synchronized from the trigger signal of the laser.

Wavelength selection of the OPO is controlled by a PDP-11/10 minicomputer. Crystal and grating are set according to values in a table, while the position of the etalon is calculated from a set of parameters. An interactive program was developed to simplify operation of the OPO LIDAR, and to make automatic measurements possible. Besides service routines for calibration and alignment of the OPO, the program enables automatic scans of the OPO, increasing or decreasing the wavelength in predetermined steps. In another mode the program tunes the OPO between two or three predetermined wavelengths, averages the received signals from each wavelenth and also calculates the rms-variation of this average for later error analysis. It then calculates the concentration of a pollutant using eqn.(2). This value is displayed in real time as well as stored for later use. This control routine proved to be essential for the measurements reported in later sections of this paper.

Without the etalon in the cavity, the OPO can be scanned under computer control continuously from 1.4 to 4.0 μm, a range of more than 4500 cm^{-1}. Fig.3 shows an example of the scan capabilities of the OPO. In the lower trace it shows an atmospheric transmission spectrum from 31 May 1979. We used a building 775 m away as backscattering target, so the total atmospheric pathlength is 1.55 km. The scan covers a 450 cm^{-1} range from 2850 to 3300 cm^{-1}, which includes numerous absorption lines mainly due to water vapor and methane, although many other trace constituents have absorption lines in this region. To confirm the accuracy of our scan and to identify lines we use the AFCRL data base[18]. The upper trace in fig.3 shows a simulated transmission spectrum using the AFCRL data. For this simulation we assumed 6 torr H_2O and 3 ppm CH_4 in the atmosphere. The linewidth was assumed to be 1.5 cm^{-1} However, the program that calculates the transmission from the AFCRL data uses a rectangular slit function, which is not a very good approximation of the OPO lineshape, and results in discrepancies between the calculated and the observed spectrum. But the general agreement of both traces in fig.3 confirms the usefulness of the OPO-source for spectroscopic applications.

It is considerable more complex to control continuous scans with the etalon inserted into the OPO cavity. Grating and etalon position have to be synchronized to within 0.1 cm^{-1}. This requires excellent stability of the tuning mechanism. Furthermore, if a scan over more than one free spectral range of the etalon is required, the etalon has to be reset to its zero position during the scan. The length of a scan is determined by the accuracy with which the etalon free spectral range and the tuning rate of the grating are known. We developed extensive software to measure semi-automatically the etalon parameters and so enable scans over many etalon free spectral ranges. We demonstrated scans over more than 10 free spectral ranges, which in the case of a 2 mm thick fused silica etalon is about 20 cm^{-1}. For our applications, this scan range is more than adequate. Fig.4 demonstrates the scanning capabilities and the linewidth of our OPO source with and without intracavity etalon. It shows the spectrum of the Q-branch of the $2\nu_3$ overtone transition in CH_4 at low pressures obtained in a photo acoustic cell

[see also the high resolution spectrum obtained by Bobin[19]]. The resolution of the OPO with and without the etalon inserted is apparent. The etalon narrowed the OPO linewidth to 0.08 cm^{-1}.

The reliability of the Nd:Yag OPO transmitter has been demonstrated by more than a year of operation without damage to the pumplaser or the OPO. Since the LIDAR consists only of solid state components, no periodic maintenance is required.

III. METHANE MEASUREMENTS

We selected the measurement of methane concentration to demonstrate the reliability of our system. The atmospheric methane concentration is recorded at the Bay Area Air Quality Management District point monitoring station in Redwood City 10 km from our laboratory. This allows the possibility of comparing the accuracy of our system with an independent station.

Fig.5 shows two transmission spectra near the CH_4 absorption region at 3.4 μm. Both spectra were obtained with the idler output of the OPO/OPA. The linewidth of the output was 1.4 cm^{-1}. The upper trace shows the atmospheric transmission between our system and a building at 775 m distance, which was used as non cooperative backscattering target. Both CH_4 and H_2O absorption lines are present. To clearly identify the CH_4 lines and to aid in selecting a transition that is free of water vapor interference, an absorption spectrum of CH_4 was measured in the laboratory. A section of the scan centered on the P-branch is also shown in the lower trace in Fig.5. The two scans in this figure can be overlaid to show that the P(2), P(7), P(9) and P(10) methane transitions are nearly water vapor free. Additional confirmation is also obtained from the spectroscopic information in the AFCRL data[18]. The ability to select interference-free absorption bands and to verify the location of spectral lines by scanning the spectrum is a major advantage of the tunable source.

We selected the P(10) transition for our measurements because it has the proper absorption strength for CH_4 measurements over the selected 775 m long path. For measurements over shorter paths, the P(7) line with a much larger cross section can be used. The computer was programmed to tune on and off the P(10) line every 20 pulses or 2 seconds. The data were normalized and processed to show the concentration of methane. An effective cross section for the CH_4 P(10) line was used based on the resolution of the OPO/OPA source. To correct for any long-term drift, the cross section was measured continuously during a run by the photo acoustic cell. The measured value of the cross section was used to calculate the methane concentration in real time.

Fig.6 shows a segment of a 17 h CH_4 measurement run. Here, the raw measurements are shown for 20 shots/line averaging or 4 sec per point. The rms fluctuations are calculated to be 0.6 ppm. To improve the precision of the measurement, longer averaging times can be used. The heavy line in Fig.6 shows the same data after later averaging to increase the relative accuracy to 0.09 ppm. The time resolution is 80 sec. per point in this case.

Fig.7 shows the full 17 hour long measurement during which the system was operating automatically under computer control. During the measurements concern developed that the mesasured CH_4 levels were high since the global average CH_4 level is close to 1.5 ppm. Hourly CH_4 average measurements were obtained from the Redwood City Bay Area Air Quality Management District point monitoring station 10 km from our lidar at Stanford. The concentration measurements from this point monitoring station are indicated by open circles in Fig.7.

The agreement between the concentration values from both measurements is as good as it can be expected considering the physical seperation between Stanford Lidar system and the Redwood City monitoring station.

To check further on the correlation between the Stanford and the Redwood City station measurements, a second extended CH_4 measurement was made on June 6, 1979. Fig.8 shows the results. In this case, the wind was blowing down the bay from Redwood City toward Stanford. The wind velocity and distance gave a 20- to 30- min delay time from Redwood City to Stanford. This delay correlates with the peak CH_4 mesurement at 2200 at Redwood City and at Stanford at 2230. Later in the evening when the wind ceased, Stanford measurements became independent of the Redwood City station measurements.

These measurements demonstrate the reliability and accuracy of remote air pollution measurements. Other pollutants with absorption lines within the tuning range of the OPO source can be measured with the same relative accuracy. The measurement of other species is discussed in section V.

IV. TEMPERATURE MEASUREMENT

For accurate pollutant measurements it is important to determine the temperature of the pollutant, since the absorption cross section is temperature dependent. This effect is usually neglected for the measurement of pollutants at atmospheric temperatures. However for emissions from sources at elevated temperatures the temperature correction can become very important. By properly selecting appropriate lines of a molecular species it is possible to make remote temperature and concentration measurements of the species simultaneously.

A number of groups have proposed and analyzed methods of making remote temperature measurements, and preliminary remote temperature measurements have been reported using Raman LIDAR[20] and a two frequency absorption measurement[21]. Remote temperature measurements using atmospheric transmittance measurements of three wavelengths have been analyzed by Mason[22], Schwemmer and Wilkerson[23]. The temperature dependence of the absorption cross section is given by the Boltzmann distribution and a partition function Q(T) as

$$\sigma(\nu_i,T)= \sigma(\nu_i,T_0)Q(T)\exp\{(E^0{}_i/k)(1/T_0-1/T)\} \qquad [3]$$

for an arbitrary reference temperature T_0, where $E^0{}_i$ is the lower state energy of the transition at frequency ν_i, and k is the Boltzmann constant.

Measuring the absorbance

$$A(\nu_i,T) = N\,\sigma(\nu_i,T)R$$

for two lines of one species with different lower state energy $E^0{}_i$ we can use eqn.(3) to determine the temperature T as

$$T= \frac{T_0}{1-\frac{kT_0}{E^0{}_1-E^0{}_2}\left\{\ln\left(\frac{A(\nu_1,T)}{A(\nu_2,T)}\right)-\ln\left(\frac{\sigma(\nu_1,T)}{\sigma(\nu_2,T_0)}\right)\right\}} \qquad [4]$$

This expression simplifies for $T-T_0 \ll T_0$ to

$$T=\frac{kT_0^2}{E^0{}_1-E^0{}_2}*\ln\left(\frac{A(\nu_1,T)}{A(\nu_2,T)}\right)+D \qquad [5]$$

with

$$D=\frac{kT_0^2}{E^0{}_1-E^0{}_2}*\left\{\ln\left(\frac{\sigma(\nu_2,T_0)}{\sigma(\nu_1,T_0)}\right)\right\}+T_0$$

The constant D can be found either using spectroscopic data, or it can be determined empirically with calibrated temperature measurements. Once the

temperature and so the cross section is known, it is straightforward to calculate the density of the species using eqn.(2).

The accuracy of a remote temperature measurement is determined by the signal to noise ratio (SNR) and the number of averaged signals (n) . From eqn.(5) one finds that

$$\delta T = \frac{kT_0^2}{E^0_1 - E^0_2} * \frac{1}{SNR\sqrt{n}} * \left\{ \sum_{i=1}^{2} \left(\frac{1+\exp(2A(\nu_i,T))}{A^2(\nu_i,T)} \right) \right\}^{\frac{1}{2}} \quad [6]$$

δT is minimized for $A(\nu_i,T) \approx 1.1$, where Eqn.(6) simplifies to

$$\delta T \approx 4 * \frac{kT_0^2}{E^0_1 - E^0_2} * \frac{1}{SNR\sqrt{n}} \quad [7]$$

For an atmospheric temperature measurement, we selected H_2O as absorbing species for the following reasons:

- H_2O allows simultaneous measurement of temperature and humidity, an important capacity for remote metereological measurements.
- Due to the complexity of the H_2O spectrum, nearby lines with a large lower state energy difference can be found. This simplifies the measurement since the transmitter has to be tuned only over small wavelength increments.
- Lines generating the appropriate absorbance to minimize eqn.(6) for different pathlengths can be found.

We used the AFCRL-tapes[18] to select appropriate H_2O lines for temperature and humidity measurements over a 755 m long path [for a discussion of this line selection see ref.24]. We selected two lines of the 1.9 µm H_2O band at 5650.41 cm^{-1} and 5651.33 cm^{-1}. The difference in lower state energy is 1456 cm^{-1}. From eqn.(7), we estimate a temperature accuracy of 1°C for a product of $SNR\sqrt{n}=175$. For a SNR of 25, this means a 50 shot average, which promises a good time resolution for this measurement.

The lower trace in Fig.9 shows an atmospheric transmission scan with a 0.1 cm^{-1} resolution tuned over a 17 cm^{-1} range around the selected lines. The upper trace is a simulated transmission spectrum, using AFCRL-tapes[18]. We used scans similar to this to calibrate the tuning of the OPO and to identify the temperature sensitive lines.

Once the wavelength of these lines is determined and the OPO aligned, measurements of temperature and humidity are done under computer control. The return signal at each frequency is averaged over several shots before tuning to another wavelength. To keep errors due to water vapor fluctuations small, it is desirable to tune the OPO after each shot and average the temperature data afterwards. However, tuning between different wavelengths takes up to 0.5 sec. To improve the time resolution of our measurements we average 30 shots per line before tuning to the next line. When all three required wavelengths are probed, temperature and humidity are calculated. This cycle continues, until a total number of 150 shots per line is reached. Then the computer calculates the average of five temperature and humidity data points as well as the error due to return signal fluctuations, stores and displays those values.

Fig.10 shows the record of temperature and humidity from the morning of the 11th March 1980. Each point represents an average of 150 shots/line, or a time resolution of 45 sec. The outside weather was cloudy at first, with rain starting at 0740. The rain increased until it was so strong at 0810 that the measurement had to be interrupted. At 0820 the rain stopped, the cloud cover slowly dissipated, and the wind increased. The remotely measured temperature is compared with a record of a

thermograph at the telescope. The general agreement is good. Some discrepancies of the two measurements are expected since the remote measurement averages over a path from 10 to 60 m above the ground and 775 m length, while the thermograph is located on the roof of a building. The rms-deviation for each temperature measurement is calculated from the return signal fluctuations. It varies with the metereological conditions: in the early morning, the SNR was measured to be 25. The variance of the temperature measurements then is 1.1°C, which is only slightly worse than the estimate in eqn.(7). The SNR decreases later due to the rain, and accordingly the rms-deviations increase to 1.6°C. After the rain stopped, the SNR improved again to about 25. However, the temperature uncertainety stays at 1.5°C The reason for this increased error can be found in the stronger humidity fluctuations due to the wind. Any variation in absolute humidity during the 10 sec. measurement cycle for each temperature point increases the uncertainety of this measurement. Shorter measurement cycles will improve the accuracy of the measurement.

The calibration of our temperature data is done by minimizing the difference between the remote temperature data and the thermograph data. We have collected more than 10 hours of temperature data, and have determined a value for the constant D as 35°C, which is 19°C less than predicted from the available spectroscopic data.

We have demonstrated the feasibility to measure temperature and humidity simultaneously. The 1.9μm H_2O band makes temperature measurements with 1.0°C accuracy possible. For the present measurements of atmospheric temperature the selected lines are optimal. However, for temperature measurements at elevated temperatures such as encountered in stack exhausts a different selection of lines has to be made.

V. MEASUREMENT OF OTHER ATMOSPHERIC TRACE CONSTITUENTS

In this section we discuss the possibility of measuring other trace constituents in the atmosphere with the OPO LIDAR. Most pollutants have absorption bands in the 1.4 to 4.0 μm tuning range of the OPO. However, some of the lines are too weak to measure atmospheric concentrations, while others lie in regions of strong water vapor absorption, which makes measurements over long paths impossible.

To estimate the sensitivity of a measurement of a certain species it is assumed that a 1% change in transmission can be measured. For the reported measurements this is true for averages between 150 laser pulses per line for the H_2O measurements, to 2000 pulses per line for the CH_4 measurements, which means averaging times between 30 and 400 sec. The variation of the averaging time is due to the variation of the output energy and pulse to pulse stablilty of the OPO over its tuning range, but also due to water vapor continuum absorption around 3.4 μm[18].

We discuss measurement capabilities of the major pollutants as identified by Wright et al. in ref.25. Spectroscopic information was obtained from different sources, the AFCRL data base[18] being the most important one since it contains the major atmospheric constituents and is ideally suited to check for interferences of different species. An overview over the measurement capabilities is summarized in table 2.

H_2O: The influence of water vapor on atmospheric processes and measurements is so important, that it must be discussed first. The measurement of humidity is easily possible in the infrared, as was demonstrated in section IV. A large number of lines exists, which makes it possible to select one with the ideal cross section for a specific measurement. The two water vapor absorption bands of importance for measurements

with the OPO transmitter are the 1.9 μm and 2.7 μm bands. These bands absorb so strongly, that measurements over long paths in the regions from 1.8 to 2.0 μm and 2.4 to 3.2 μm are not possible. The surrounding regions contain lines of ideal strengths for atmospheric humidity measurements. The large number of water vapor lines leads to interference problems in the measurements of many other pollutants. Thus it is necessary to measure the absolute humidity first in order to correct absorption measurements on pollutant lines influenced by nearby H_2O lines.

CO_2: On a global scale, carbondioxide is important to monitor due to its effect on the thermal balance of the atmosphere[26]. On a local scale, CO_2 can be used as a tracer for emissions from combustion processes, and to measure the temperature of these emissions. The atmospheric background of CO_2 is 330 ppm in an unpolluted atmosphere, and ranges up to 350 ppm in polluted regions. For remote measurements with the OPO transmitter, the $\nu_1+2\nu_2+\nu_3$ -combination band at 4983 cm^{-1} is ideal. Using the AFCRL data base[18] and our own atmospheric transmission spectra we determined that the P(8), P(10) and P(36) lines are interference free from water vapor absorption. These lines are well suited to measure atmospheric background as well as source emissions of CO_2. Using the 570 cm^{-1} lower level energy difference of the P(8) and the P(36) lines, temperature of sources can be determined with a 5°C accuracy.

CO: Carbon monoxide is known to be a health hazard in high concentrations. The Clean Air Act sets the CO exposure limit to an average value of less than 35 ppm over one hour or 9 ppm over 24 hours. Remote monitoring simplifies the task of measuring ambient concentrations and emissions. Measurements of CO with the OPO is possible at the overtone band at 4260 cm^{-1} [27]. Many lines without water vapor interference can be found. The absorption cross section is approximately 0.4 [atm cm]$^{-1}$ [18] which leads to a measurement sensitivity of 0.3 ppmkm. The measurement of atmospheric background concentrations of CO in unpolluted atmospheres difficult, but the observation of pollution and measurements of source emissions are possible.

SO_2: Sulfur dioxide is the major pollutant in sulfurous smog. It has been recognized as a health hazard, and the Clean Air Act requires annual average SO_2 concentrations of less than 0.03 ppm, although over a 3 hour period the average may be as high as 0.50 ppm. We have demonstrated the possiblity to measure sulfur dioxide with the OPO LIDAR earlier[12]. The $\nu_1+\nu_3$ combination band around 2499 cm^{-1} has linestrengths of 0.4 [atm cm]$^{-1}$ [28], which makes measurements of concentrations of 0.25 ppmkm possible. However, this measurement has to be made near the end of the tuning range of the $LiNbO_3$ OPO, where the energy output is low and pulse energy fluctuations are increased. Thus a large number of laser pulses have to averaged to achieve the desired sensitivity. However, measurements of source emissions and monitoring of SO_2 polluted atmospheres is possible.

O_3: Ozone is a major constituent in photochemical smog. There is a natural ozone background of 0.01 ppm, but its concentration reaches 0.3 ppm in photochemical smog[25]. Within the tuning range of the OPO, the strongest absorption band is the $3\nu_3$ band at 3050 cm^{-1} The strongest lines are about 0.3 [atm cm]$^{-1}$ [18], which leads to a sensitivity of 0.3 ppmkm. This value is not adequate to measure atmospheric ozone with the OPO LIDAR.

NO_x: Nitrogen oxides are important in photochemical smog. Their primary anthropogenic source is combustion. In polluted urban regions the concentration of NO_2 may be 0.1 ppm, or even higher in exceptional circumstances. The measurement of NO is not possible with the OPO LIDAR, since only a weak overtone trans-

ition exists at 4746 cm^{-1}. But NO_2 has relatively strong lines in the $\nu_1+\nu_3$ band at 2910 cm^{-1}. From spectra in ref.29, the strongest line has a strength of 3.2 $[atm\ cm]^{-1}$, which allows measurements with a 0.03 ppmkm sensitivity. Measurements of sources as well as monitoring of polluted regions is possible. However, potential interference from water and hydrocarbon lines makes careful line selection necessary to minimize interference with those species.

N_2O: Another nitrogen compound in the atmosphere is Nitrous Oxide. There is an atmospheric N_2O concentration of 0.29 ppm, which is mainly caused by biological action in soil. It is inert in the troposhpere but of interest due to its interaction with ozone in the stratosphere[30]. The absorption band at 2545 cm^{-1} is strong enough, to promise a sensitivity of 0.05 ppmkm, and interference free lines can be found[18]. This allows measurements of atmospheric background concentrations of nitrous oxide.

NH_3: Another pollutant of importance is Ammonia. Its strongest absorption bands within the tuning range of the OPO are around 3400 cm^{-1} [31]. However, we have not found spectra of adequate accuracy to determine, if absorption measurements are possible using lines located in the strong surrounding water vapor absorption region.

HCHO: Formaldehyde also is a component of photochemical smog. Its atmospheric concentration varies between 1 and 50 ppb[25]. The cross sections of lines around 2800 cm^{-1} from ref.29 promise a sensitivity of 0.01 ppmkm, which makes long path measurements suitable to monitor formaldehyde concentrations in smog conditions.

HCl: The natural background of Hydrogen cloride is negligibly small, but anthropogenic sources can release HCl in large quantities that lead to concentrations of 1 to 5 ppm[25]. HCl has very strong absorption lines around 2900 cm^{-1}. From the spectrum in ref.29 we determine cross sections of 10 $[atm\ cm]^{-1}$, which allows sensitivities of 0.01 ppmkm. Since several lines can be selected, interference from water vapor and hydrocarbons can be minimized. Measurements of HCl are possible with the OPO LIDAR.

Hydrocarbons: Hydrocarbons are important in photochemical processes. Only methane has a large background in unpolluted atmospheres, all other hydrocarbons arise mainly from anthropogenic sources[25]. The major sources are combustion and chemical processes. All hydrocarbons have a very strong ν_3 vibration band, but interferences with water vapor lines as well as other hydrocarbons cause problems for the measurements of some of them. Methane has a background concentration in an unpolluted atmosphere of 1.5 ppm. We have discussed the measurement of CH_4 with the OPO LIDAR in section 3 and demonstrated the sensitivity in such a measurement.

The other hydrocarbon components play a more important role in photochemical smog than methane. However, due to the difficulties to measure them independently, little is known about reactions of specific components in the atmosphere. With the OPO LIDAR a large number of hydrocarbons can be measured with good sensitivity. However, water vapor, methane and other components all have to be measured simultaneously due to interference of lines. Using high resolution spectra obtained with the EPA ROSE System[32], we identified measurement possibilities for Ethane, Propane and Ethylene.

Ethane can be measured at 2976.8 cm^{-1}, where it has an absorption line with a strength of 13 $[atm\ cm]^{-1}$. This line is overlapped by a water vapor line, but transmission on this wavelength is adequate for the use of long paths. This line promises a sensitivity of 8 ppbkm, if errors due to the measurement of H_2O concentration can be neglected.

Propane has a very strong line at 2967.6 cm^{-1}, the absorption cross sec-

tion was determined as 83 [atm cm]$^{-1}$. However, H_2O, CH_4, and other hydrocarbons have absorption lines close to this wavelength, and their interference reduces the sensitivity. But a 10 ppbkm sensitivity still can be expected.

Ethylene has a relatively strong line at 2980 cm^{-1}, but this line is completely obscured by a strong water vapor line. Measurement is possible at 2962.5 cm^{-1}, but linestrength here is only 1.7 [atm cm]$^{-1}$, which does not promise the measurement of traces in the atmosphere.

Other hydrocarbon components have to be evaluated in detail.

VI. CONCLUSIONS

We demonstated the capabilities of a $LiNbO_3$ OPO as a LIDAR transmitter. The OPO has a tuning range of 4500 cm^{-1} from 1.4 to 4.0 µm. The linewidth is less than 1 cm^{-1}, and can be reduced to 0.1 cm^{-1} by insertion of a tilted etalon. Wavelength selection of the OPO is done under computer control. An extensive software routine was developed to control automatic measurements.

Reliability of the system was demonstrated in a series of remote methane measurements at 3.4 µm over a 775 m long atmospheric path, using a building as non cooperative backscattering target. The longest of these measurements was over a period of 18 hours, during which the system operated automatically under computer control. Our concentration measurements were compared with those of a nearby point monitoring station. The agreement was excellent.

The advantages of a continuously tunable infra red transmitter were further demonstrated with a measurement of metereological importance. We measured simultaneously average temperature and humidity over the 775 m long path. We selected for this measurement two nearby lines in the 1.9 µm water band, which have a 1456 cm^{-1} lower level energy difference and so promise a good temperature sensitivity, and are of similar strength. Using those lines, we measured temperature with a 1°C relative error, while humidity data have a relative error of 1%.

In addition to the described measurements, a large number of other trace constituents can be measured. We used available spectroscopic data to identify the sensitivity for measurements of the most important trace constituents in the troposphere. We found, that background concentrationes of some pollutants can be measured. Source emission monitoring is feasable for most important pollutants with the OPO LIDAR.

The transmitter source can be improved. An increase of output energy to more than 70 mJ is possible. With this amount of transmitted energy, depthresolved measurements using Mie scattering as distributed reflector are possible. This will have advantages for source monitoring applications. For the measurement of ambient background concentrations, however, a monostatic system like the one described here promises the highest sensitivity.

ACKNOWLEDGEMENTS

We want to acknowledge helpful discussions with E.R.Murray of SRI International and W.F.Herget of E.P.A. We want also acknoledge the loan of the receiving telescope by EPRI and support for this program by ARO under the contract #DAAG29-77-G-0181.

REFERENCES

[1] E.D.Hinkley ed.: "Remote Probing of the Atmosphere" Springer Verlag, Berlin 1976

[2] H.Kildal, R.L.Byer: "Comparison of Laser Methods for Remote Detection of Atmospheric Pollutants", Proc.IEEE 59, p.1633-1644, 1971

[3] R.L.Byer, M.Garbuny: "Pollutant Detection by Absorption Using Mie Scattering and Topographic Targets as Retroreflectors" Applied Optics 12, p.1496-1505, 1973

[4] R.L.Byer, E.R.Murray: "Remote Monitoring Techniques" in "Handbook of Airpollution Analysis", ed.R.Perry and R.Young, Chapman Hall, London, 1977

[5] K.W.Rothe, U.Brinkmann, H.Walther: "Applications of Tunable Dye Lasers to Air Pollution Detection: Measurement of Atmospheric NO_2 Concentrations by Differential Absorption", Appl.Phys.3, p.115-119, 1974

[6] W.B.Grant, R.D.Hake Jr., E.M.Liston, R.C.Robbins, E.K.Proctor Jr.: "Calibrated Remote Measurement of NO_2 Using the Differential Absorption Backscatter Technique", Appl.Phys.Lett.24, p.550-552, 1974

[7] K.Frederikson, B.Galle, N.Nystrom, S.Svanberg: "A Mobile LIDAR System for Measurements of NO_2, SO_2, O_3, and particles" IX ILRC, Munich, 1979

[8] J.G.Hawley, L.D.Fletcher, G.F.Wallace, M.Herron: "A Mobile Differential Absorption Lidar (DIAL) for Range Resolved Measurements of SO_2, O_3, and NO_2", X. ILRC, Univ. of Maryland, 1980

[9] W.Baumer, K.W.Rothe, H.Walter: "Range Resolved Measurements of Atmospheric Pollutants", IX ILRC, Munich, 1979

[10] D.K.Killinger, N.Meynuk, W.E.DeFeo: "Remote Sensing of CO Using Frequency-Doubled CO_2 Laser Radiation", To be published in Appl.Phys.Lett.

[11] J.Altmann, W.Lahmann, C.Weitkamp: "Remote Measurement of Atmospheric N_2O with a DF Laser Lidar", Applied Optics, to be published

[12] R.A.Baumgartner, R.L.Byer: "Remote SO_2 Measurements at 4 μm with a Continuously Tunable Source", Optics Letters 2, p.163-165, 1978

[13] R.A.Baumgartner, R.L.Byer: "Continuosly tunable IR LIDAR with Applications to Remote Measurements of SO_2 and CH_4", Applied Optics 17, p.3555-3561, 1978

[14] S.J.Brosnan, R.L.Byer: "Optical Parametric Oscillator Threshold and Linewidth Studies", IEEE Journ. Quant. Electr. QE-15, p.415-431, 1979

[15] R.A. Baumgartner, R.L.Byer: "Optical Parametric Amplifiers", IEEE Journ. Quant. Electr. QE-15, p. 432-444, 1979

[16] M.Endemann, R.L.Byer: "Remote Probing of Atmospheric Methane over Long Timescales Using a Widely Tunable Source", Post Deadline Paper IX ILRC, Munich, 1979

[17] G.K.Klauminzer: "New High Performance Short Cavity Dye Laser Design", Post Deadline Paper at CLEA, Washington D.C., 1977

[18] R.A.McClatchey, W.S.Benedict, S.A.Burch, R.F.Calfee, K.Fox, L.S.Rothman, J.S.Garing: "AFCRL Atmospheric Absorption Line Parameter Compilation", AFCRL Report-TR-73-0096, 1973

[19] B.Bobin: "Interpretation de la Bande Harmonique $2\nu_3$ du Methane $^{12}CH_4$ (De 5890 a 6107 cm^{-1})", Journ.du Phys. 33, p 345-352, 1972

[20] A.Cohen, J.S.Cooney, K.N.Gelleo: "Atmospheric Temperature Profiles from LIDAR Measurements of Rotational Raman and Elastic Scattering", Applied Optics 15, p.2896-2901,1979 see also, R.Gill, K.Geller, J.Farina, J.Cooney, A.Cohen, Journ. of Appl.Met. 18, p.225, 1979

[21] E.R.Murray, D.D.Powell, J.E.van der Laan: "Measurement of Average Atmpspheric Temperature Using CO_2 Laser Radar",Applied Optics 18, June 1980

[22] J.B.Mason: "LIDAR Measurement of Temperature: A New Approach", Applied Optics 14, p.76-78, 1975

[23] G.K.Schwemmer, T.D.Wilkerson: "LIDAR Temperature Profiling: Performance Simulations of Mason's Method", Applied Optics 18, p.3539-3541, 1979

[24] M.Endemann, R.L.Byer: "Remote Single-Ended Measurements of Atmospheric Temperature and Humidity at 1.9 μm Using a Continuously Tunable Source", to be published in Optics Letters, Oct.1980

[25] M.L.Wright, E.K.Proctor, L.S.Gasiorek, E.M.Liston: "A Preliminary Study of Air Pollution Measurements by Active Remote-Sensing Techniques", NASA CR-132 724, 1975

[26] F.Moeller: "On the Influence of Changes in the CO_2 Concnetration in Air on the Radiation Balance of the Earth's Surface and on the Climate", J.Geophys.Res.68, p.3877, 1963

[27] T.Henningson, M.Garbuny, R.L.Byer: "Remote Detection of CO by Parametric Tunable Laser", App.Phys.Lett.24, p.242-245, 1974

[28] A.S.Pine, P.F.Moulton: "Doppler Limited and Atmospheric Spectra of the 4 μm $\nu_1+\nu_3$ Combination Band of SO_2", Journ. of Molec. Spectro. 64, 15-30, 1977

[29] P.L.Hanst: "Spectroscopic Methods for Air Pollution Measurement", chapter in "Advances in Environmental Science and Technology, vol.2", J.N.Pitts,Jr. and R.L.Metcalf ed., Wiley Interscience, N.Y.

[30] G.L.Hutchinson, A.R.Morier: "Nitrous Oxide Emissions from an Irrigated Cornfield", Science 205, p.1125-1126, 1979

[31] G.Herzberg: "Molecular Spectra and Molecular Structure: II. Infrared and Raman Spectra of Polyatomic Molecules", D.van Nostrand Company, Inc., 1943

[32] W.F.Herget, Private Communication

	CH_4 measurement	Temperature measurement
Transmitter	OPO/OPA	OPO
Frequency range	2917-2922 cm^{-1}	5650-5652 cm^{-1}
Energy / pulse	7 mJ	5 mJ
Pulse length	10 nsec	10 nsec
Pulse rep. rate	10 Hz	10 Hz
Linewidth (FWHM)	1.4 cm^{-1}	0.1 cm^{-1}
Receiver		
Light collector	Newtonian telescope	Newtonian telescope
Diameter	400 mm	400 mm
Focal length	1.2 m	1.2 m
Detector	InSb at 77 K	InSb at 77 K
Detector D*	$1.3*10^{11}$ (cm$\sqrt{Hz}$/W)	$4*10^{10}$ (cm$\sqrt{Hz}$/W)
Electronics		
Impulse response time	300 nsec	300 nsec

Table 1: Parameters of the OPO-LIDAR

SPECIES	ABSORPTION CROSS SECTION [atm cm]$^{-1}$	AT WAVELENGTH [cm]$^{-1}$	PREDICTED SENSITIVITY [ppm km]	ATMOSPHERIC CONCENTRATIONS
CO_2	0.02	4969	2.5	background 330 ppm
CO	0.3	4285	0.3	in pollution 30-50 ppm
SO_2	0.4	2499	0.25	in sulfurous smog 1 ppm
NO_2	3.2	2913-2928	0.03	in photochem.smog 0.1 ppm
H_2O	2.3	2578	0.05	background 0.29 ppm
HCHO	≈10.	2898	0.01	in photochem.smog 0.05 ppm
HCl	≈10.	2822-2955	0.01	1-5 ppm locally
CH_4	>40.	3030-2910	0.005	1.5 ppm background
Ethane	13.	2976.8	0.010	concentration of
Ethylene	1.7	2962.5	0.060	all hydrocarbons except CH_4
Propane	>50.	2967.6	0.010	< 0.25 ppm in 3 hour average
H_2O	many different lines		1%	1-2%
Temp. using H_2O	0.005	5650,5651	1°C	

Table 2: Predicted measurement capabilities for the OPO LIDAR.

FIGURE CAPTIONS

Fig.1 Schematic of the 1.4 to 4.0 μm tunable transmitter.

Fig.2 Schematic of the electronics and data processing based on PDP-11/10 minicomputer.

Fig.3 450 cm^{-1} scan with the OPO LIDAR around 3.0 μm. The lower trace shows the measured transmission, using a building 775 m away as backscattering target. The upper trace shows a simulation of the same transmission spectrum using the AFCRL data base. A linewidth of 1.5 cm^{-1} was assumed for the simulation. But the rectangular lineshape in the simulation does not fit the OPO lineshape very well.

Fig.4 Photo acoustic spectrum of $2\nu_3$ CH_4 Q branch at 1.66 μm.. The scan is repeated with and without the tilted etalon in the OPO cavity. The linewidth of the OPO in each case is apparent.

Fig.5 Transmission spectrum around 3.4 μm. Upper trace shows the atmospheric transmission over a 1.55 km long path. The lower trace is transmission through a 1.2 m long absorption cell filled with CH_4 and N_2 and is used to identify CH_4 lines in the atmospheric spectrum.

Fig.6 One hour segment of remote methane measurement, showing CH_4 concentration vs. time. Each point represents a 20 shot or 4 sec average, and has a rms-fluctuation of 0.6 ppm. The heavy line shows same data after later averaging, reducing rms-erros to 0.09 ppm.

Fig.7 CH_4 concentration vs. time over a 17 hour period. Each point is an average over 80 sec, reducing rms-deviations to 0.09 ppm, which is less than the measured CH_4 fluctuation in the atmosphere. Open circles indicate measured concentrations in Redwood City point monitoring station.

Fig.8 CH_4 concentration vs. time. Stanford LIDAR data are compared to values from Redwood City point monitoring station 10 km away. Here a prevailing wind yielded a 30 min delay between the atmosphere at point monitoring station and its arrival in Stanford.

Fig.9 High resolution atmospheric scan over 1.55 km path. The OPO linewidth is 0.1 cm^{-1}. The OPO transmission scan (lower trace) is compared to a simulation using AFCRL tapes (upper trace).

Fig.10 Temperature and absolute humidity vs. time. Measurement from morning of 11th march 1980. Temperature data are compared with record from thermograph at receiving telescope.

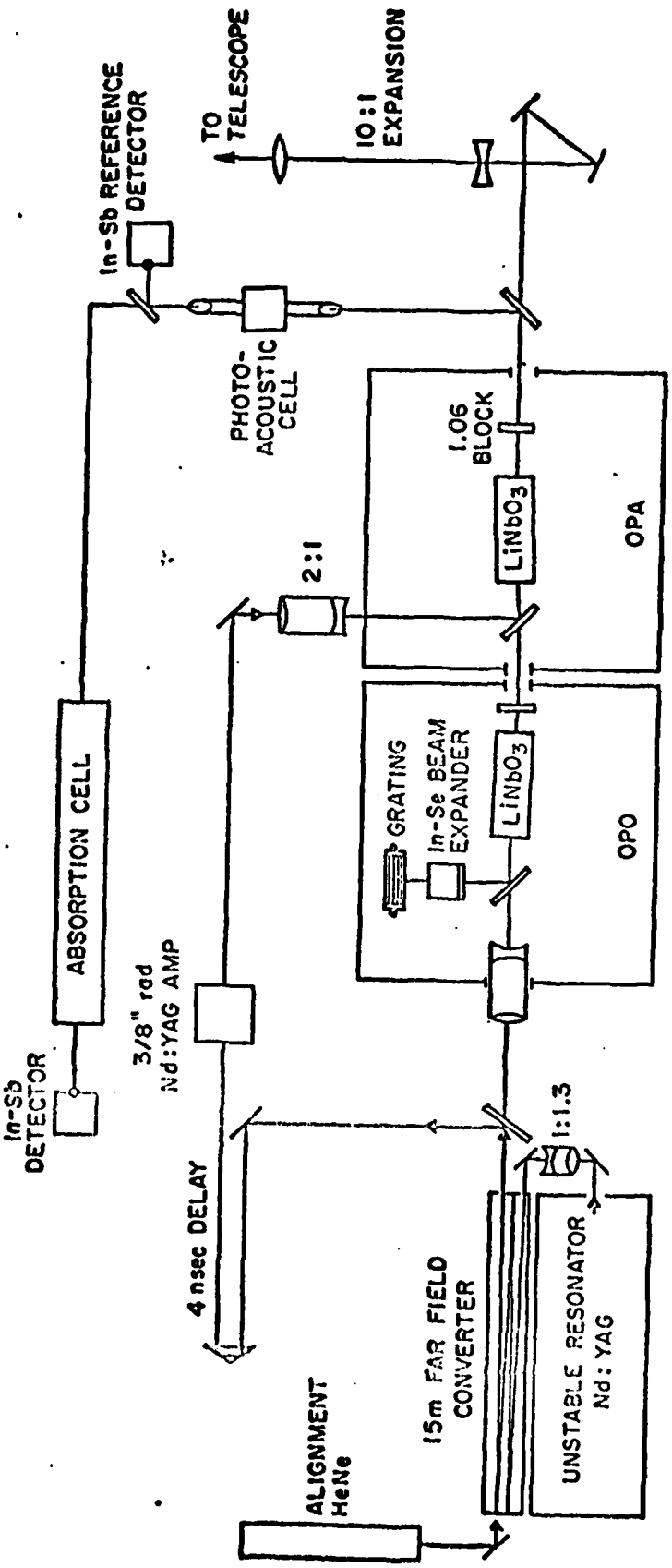

Fig.1 Schematic of the 1.4 to 4.0 μm tunable transmitter.

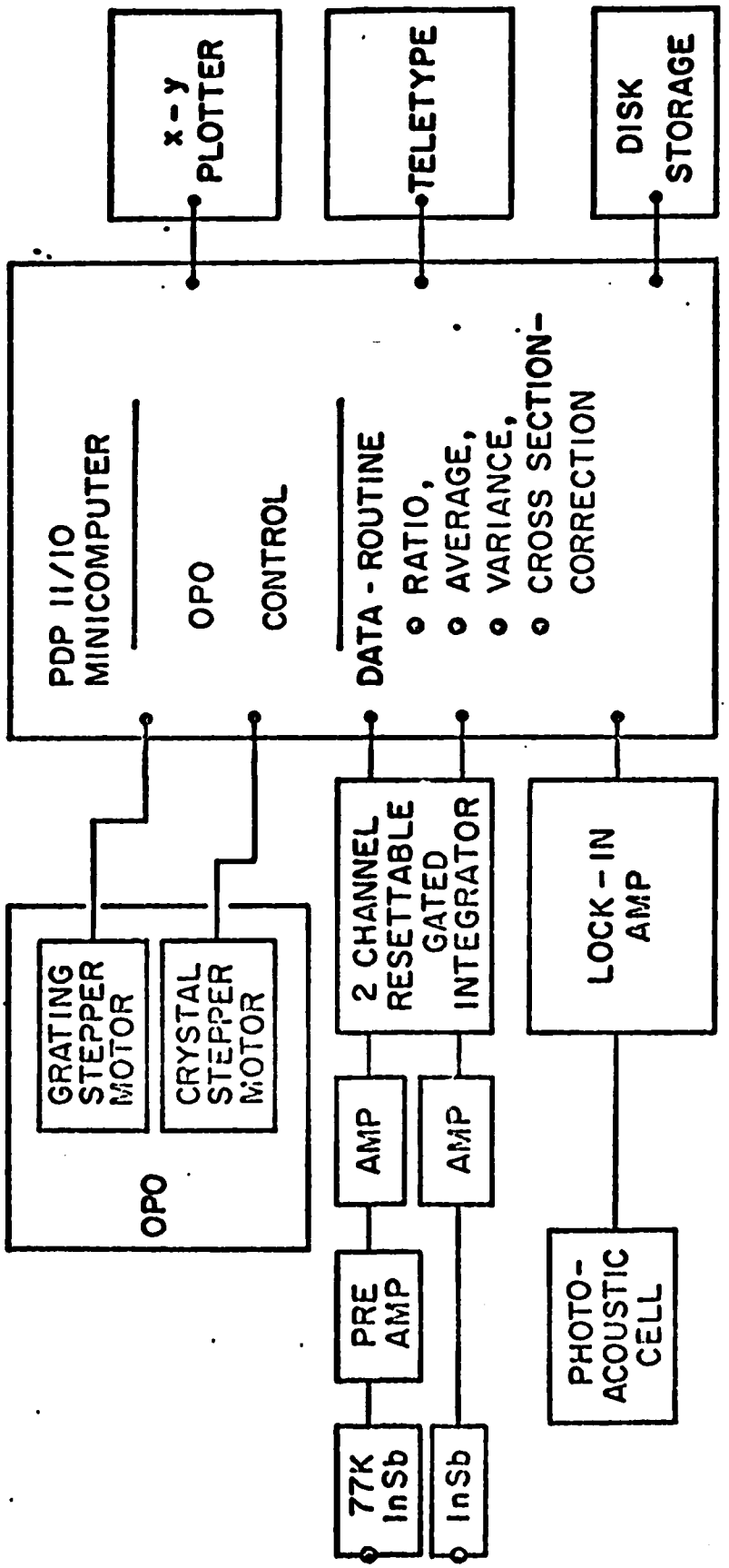

Fig.2 Schematic of the electronics and data processing based on PDP-11/10 minicomputer.

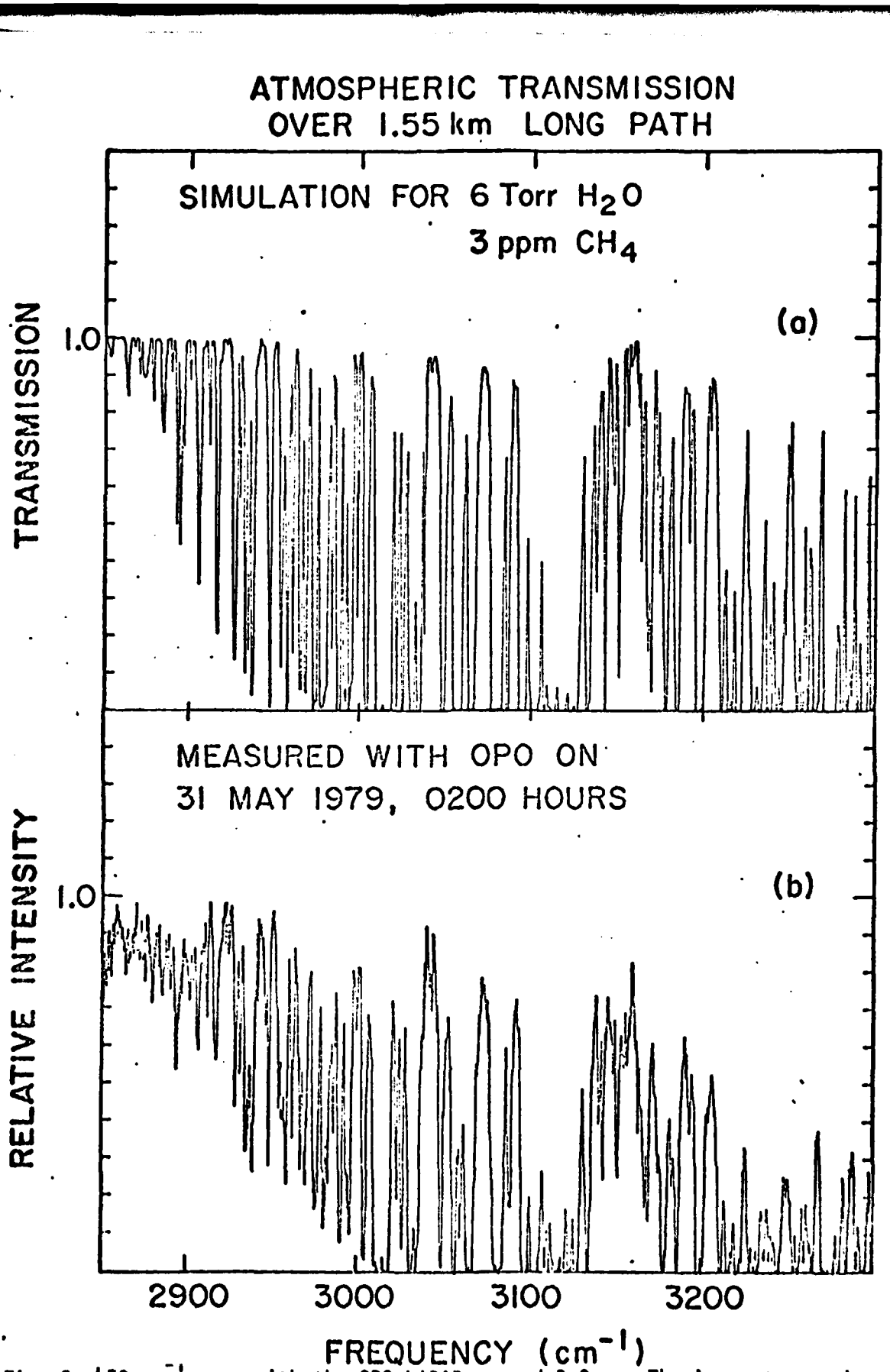

Fig. 3. 450 cm^{-1} scan with the OPO LIDAR around 3.0 μm. The lower trace shows the measured transmission, using a building 775 m away as backscattering target. The upper trace shows a simulation of the same transmission spectrum using the AFCRL data base. A linewidth of 1.5 cm^{-1} was assumed for the simulation. But the rectangular lineshape in the simulation does not fit the OPO lineshape very well.

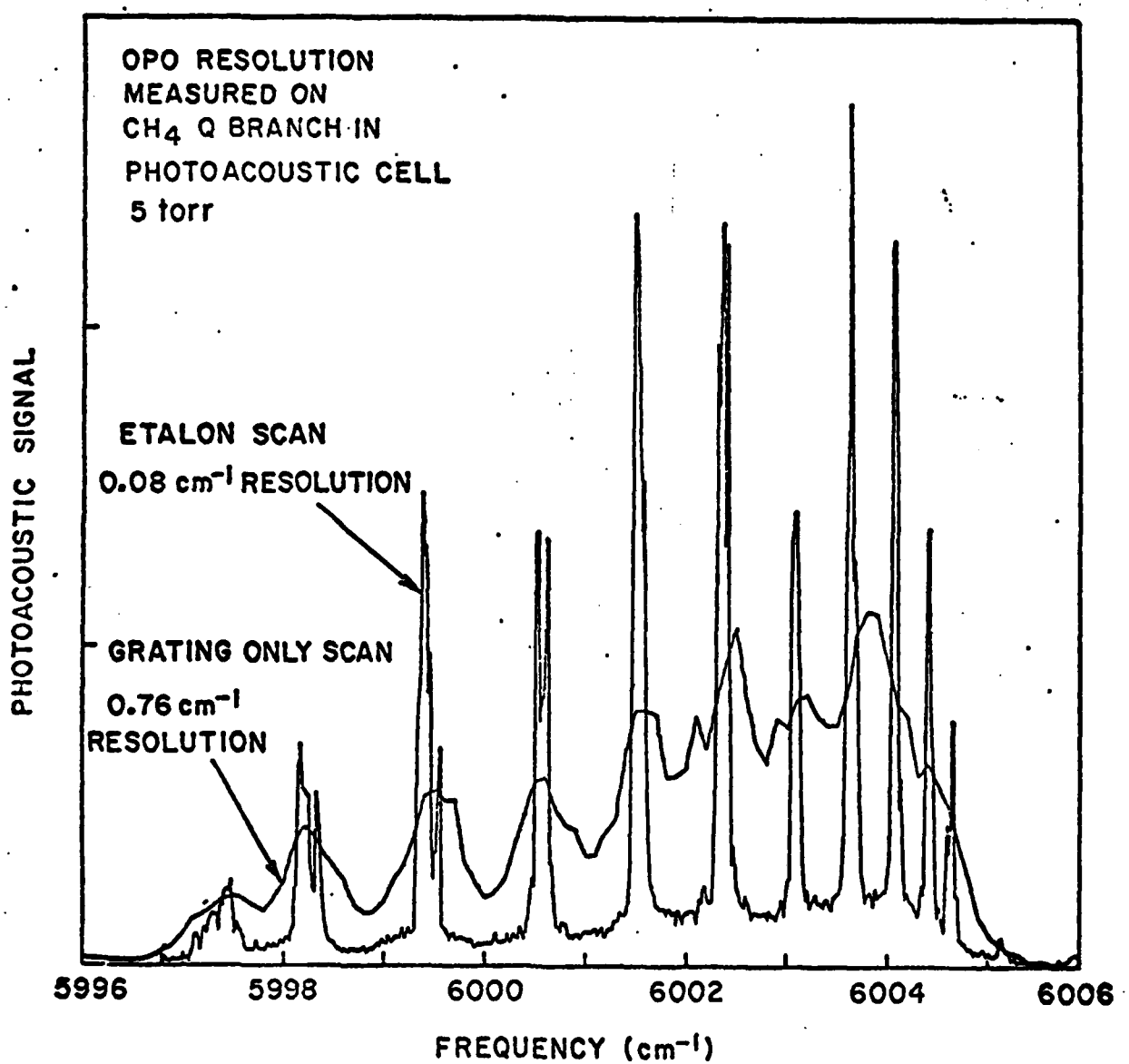

Fig. 4. Photoacoustic spectrum of $2\nu_3$ CH_4 Q branch at 1.66 μm. The scan is repeated with and without the tilted etalon in the OPO cavity. The linewidth of the OPO in each case is apparent.

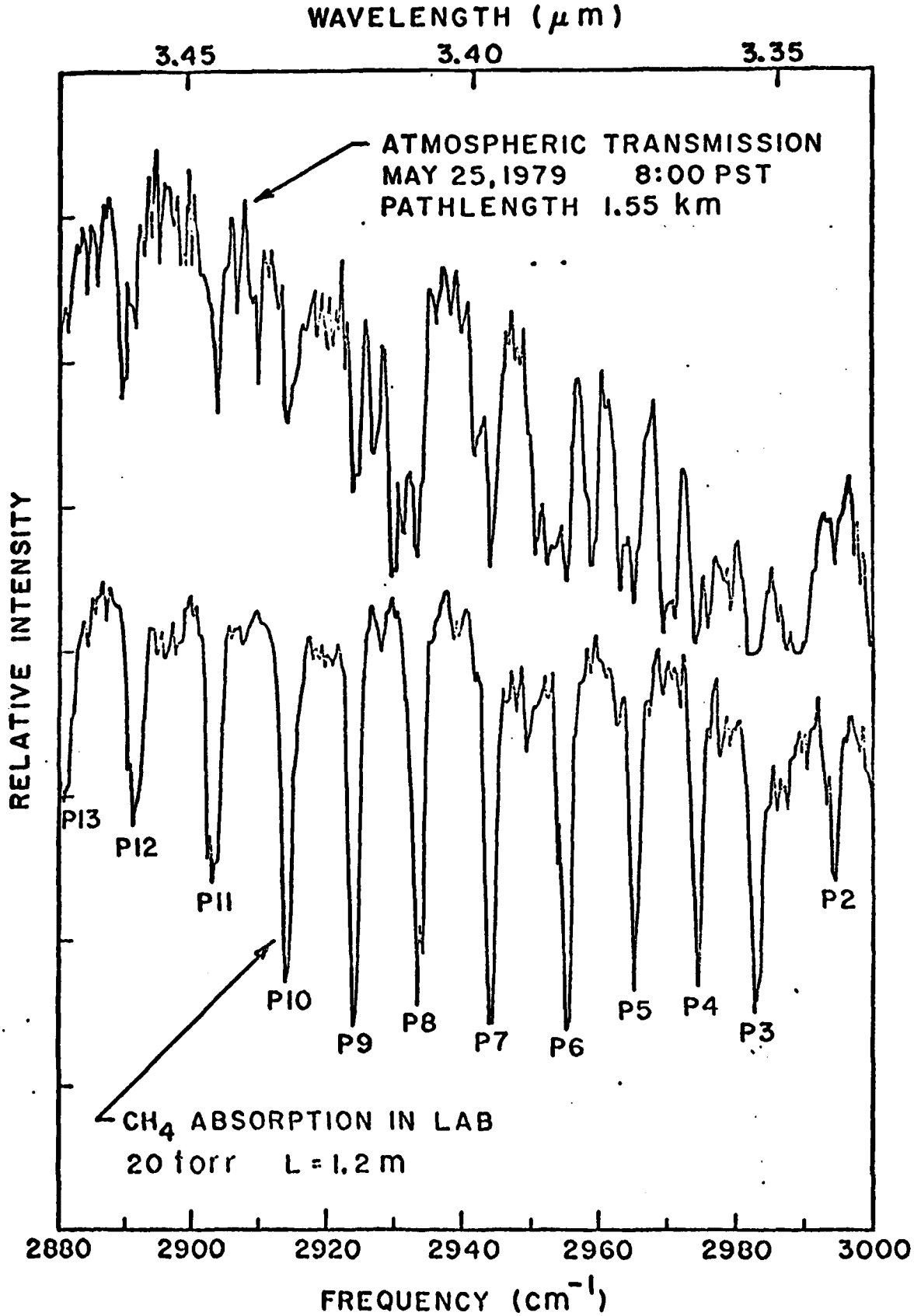

Fig. 5. Transmission spectrum around 3.4 μm. Upper trace shows the atmospheric transmission over a 1.55 km long path. The lower trace is transmission through a 1.2 m long absorption cell filled with CH_4 and N_2 and is used to identify CH_4 lines in the atmospheric spectrum.

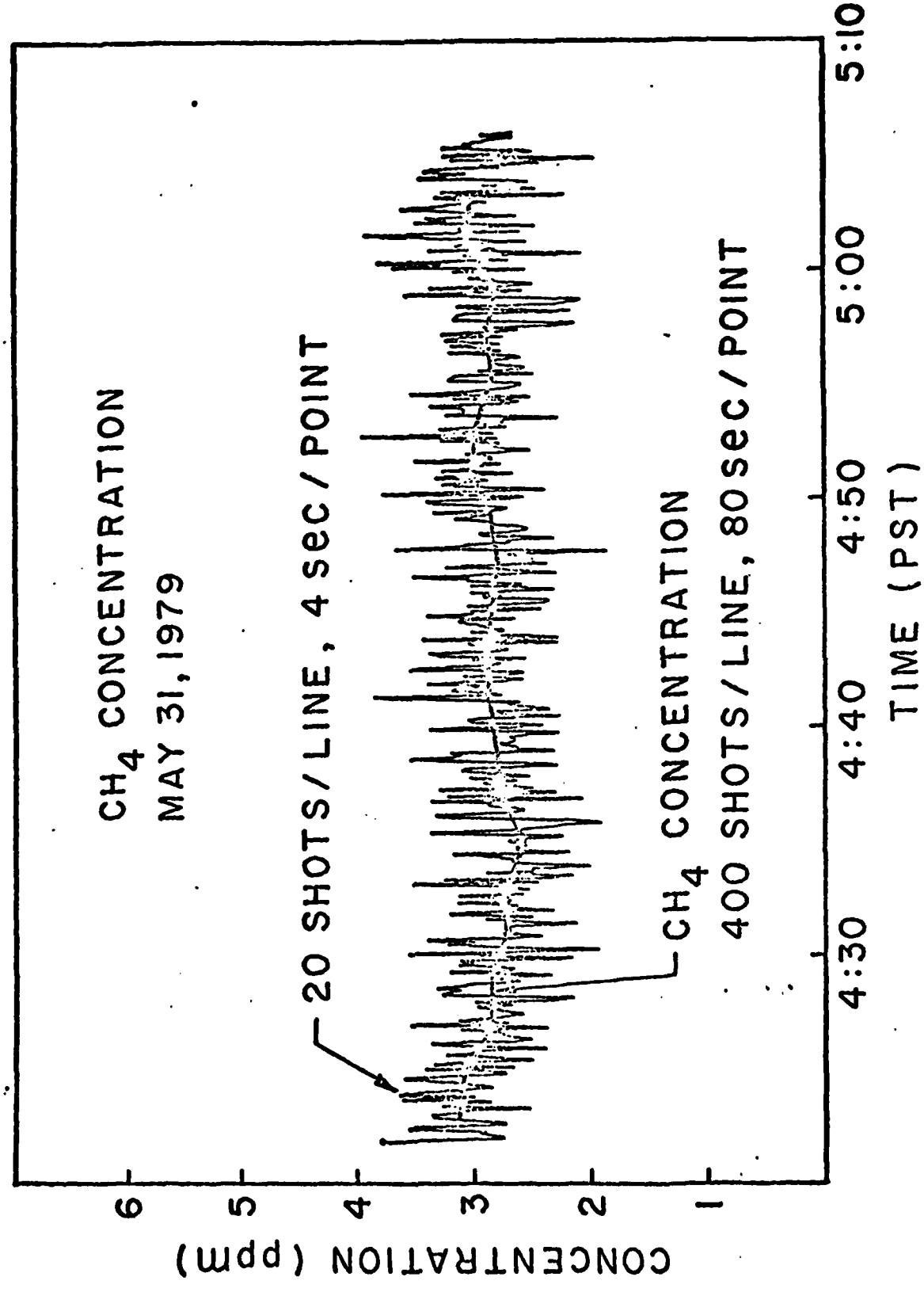

Fig.6 One hour segment of remote methane measurement, showing CH_4 concentration vs. time. Each point represents a 20 shot or 4 sec average, and has a rms-fluctuation of 0.6 ppm. The heavy line shows same data after later averaging, reducing rms-erros to 0.09 ppm.

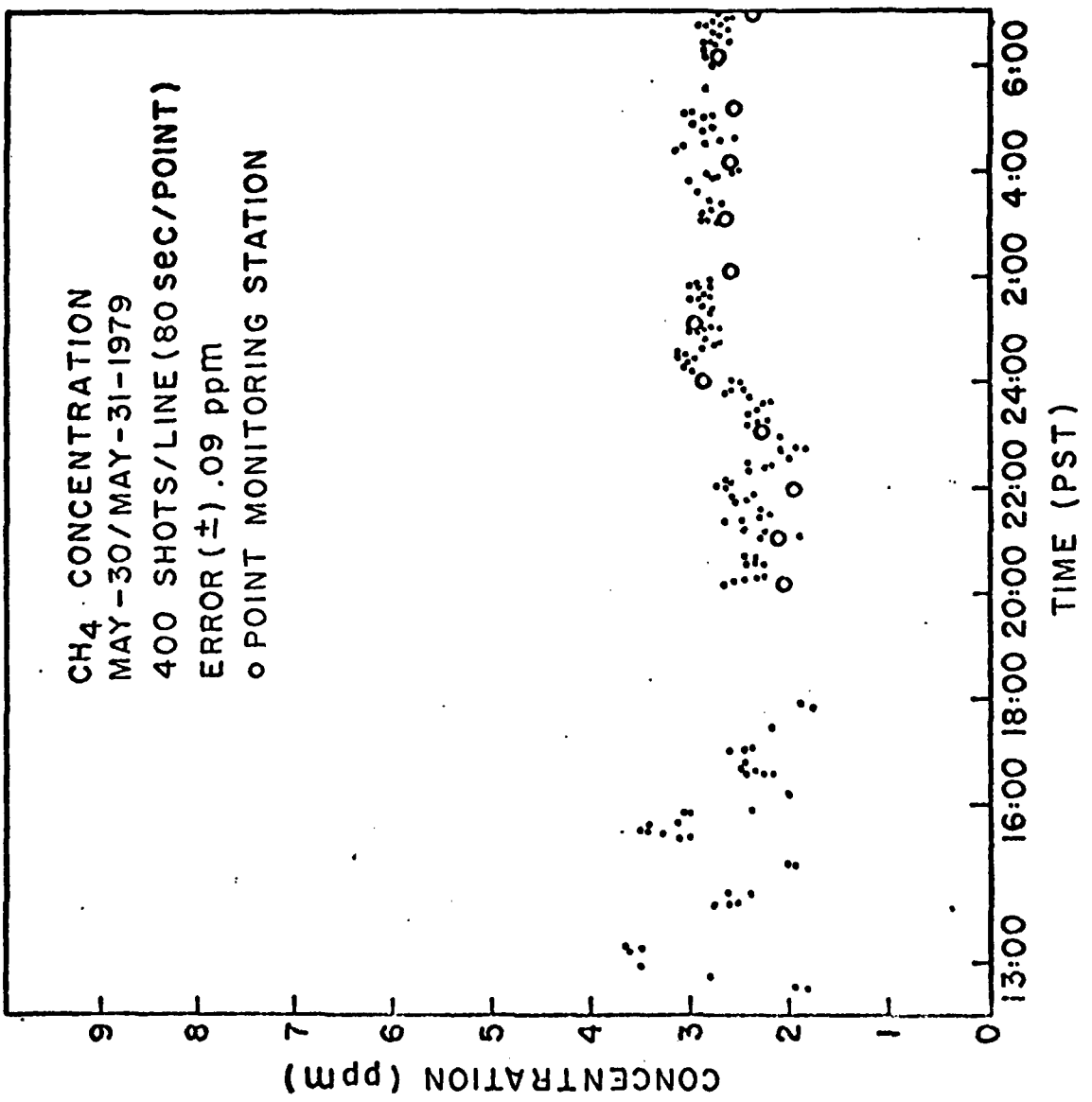

Fig.7 CH_4 concentration vs. time over a 17 hour period. Each point is an average over 80 sec, reducing rms-deviations to 0.09 ppm, which is less than the measured CH_4 fluctuation in the atmosphere. Open circles indicate measured concentrations in Redwood City point monitoring station.

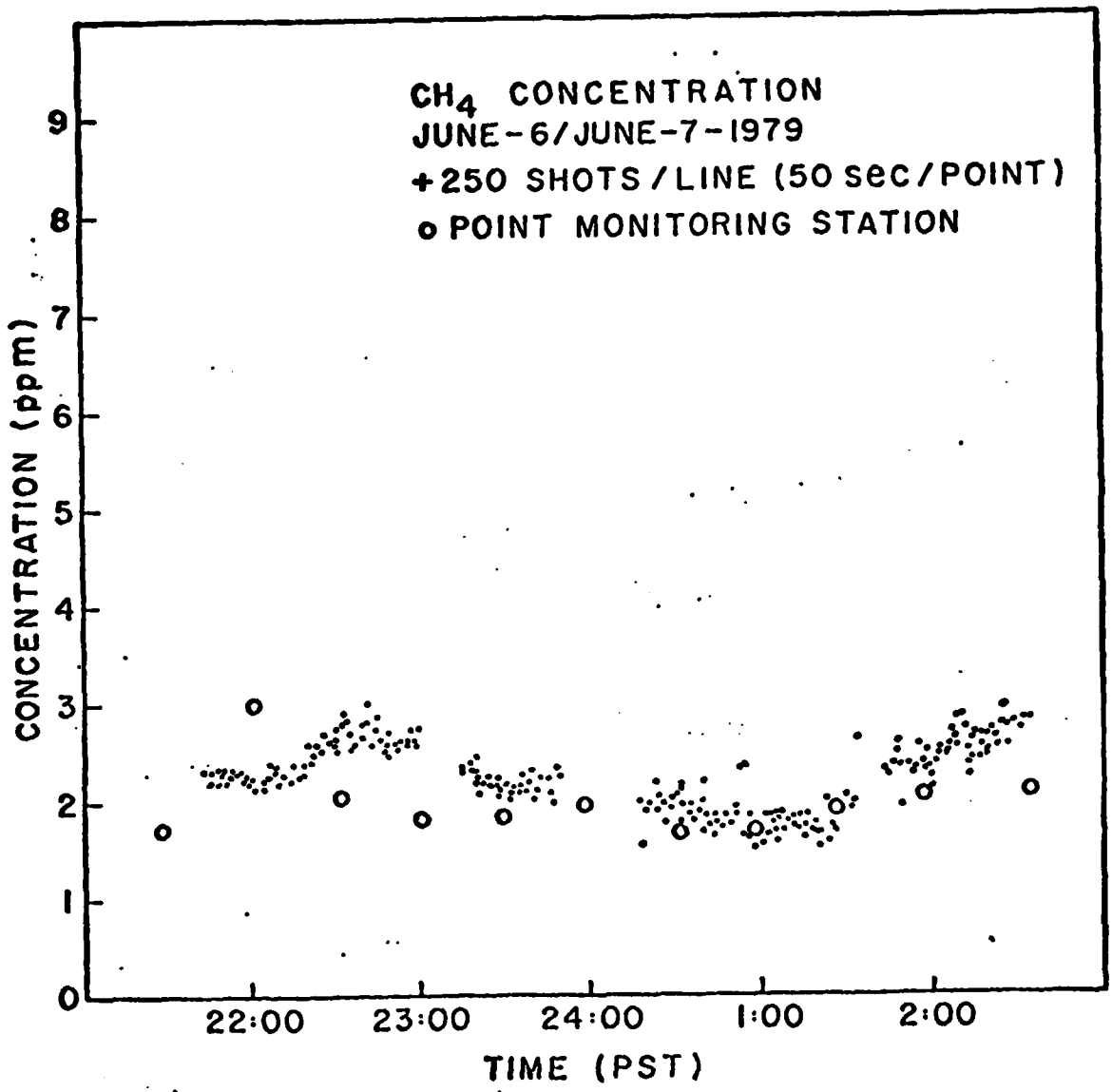

Fig.8 CH_4 concentration vs. time. Stanford LIDAR data are compared to values from Redwood City point monitoring station 10 km away. Here a prevailing wind yielded a 30 min delay between the atmosphere at point monitoring station and its arrival in Stanford.

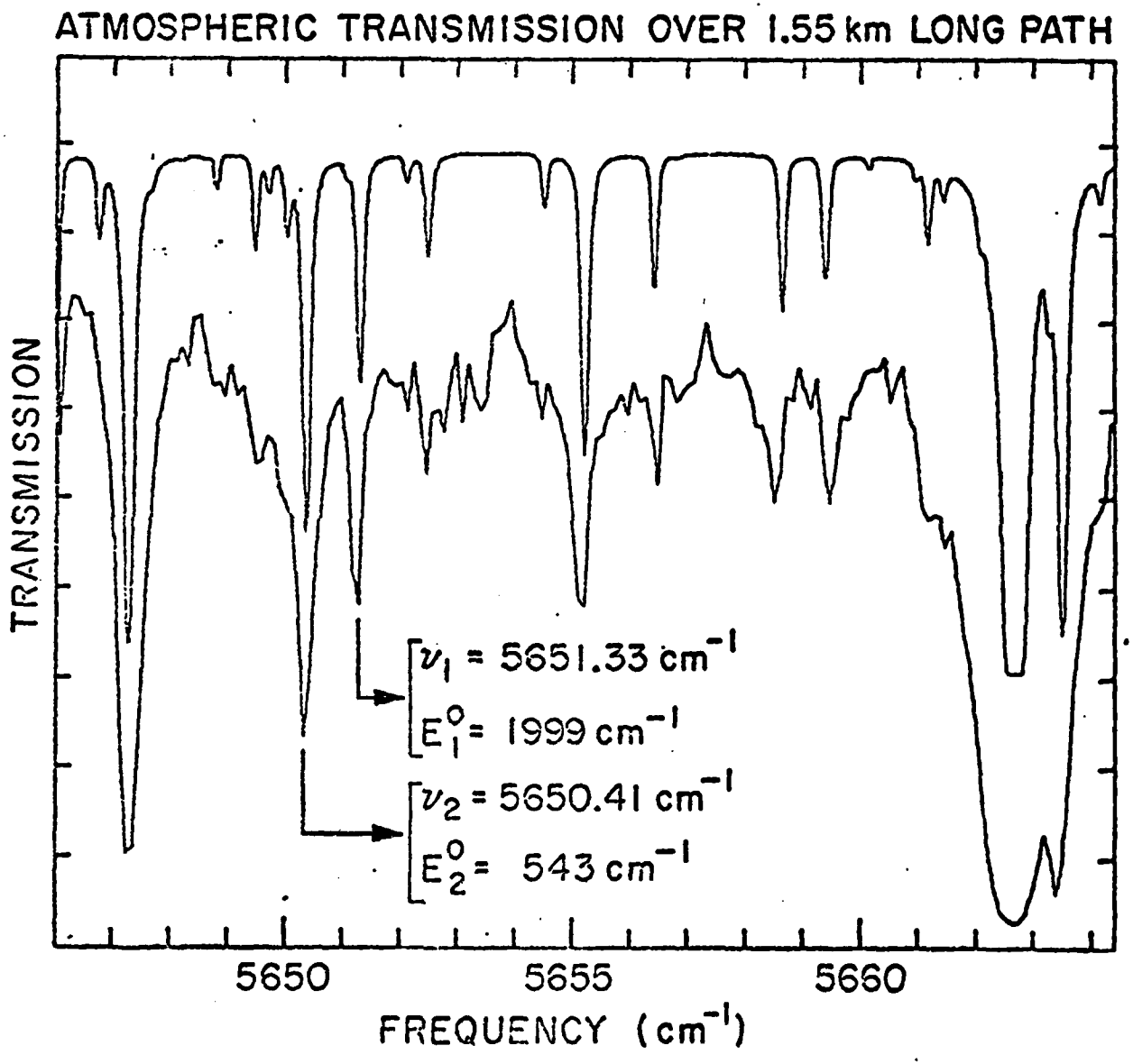

Fig. 9. High resolution atmospheric scan over 1.55 km path. The OPO linewidth is 0.1 cm^{-1}. The OPO transmission scan (lower trace) is compared to a simulation using AFCRL tapes (upper trace).

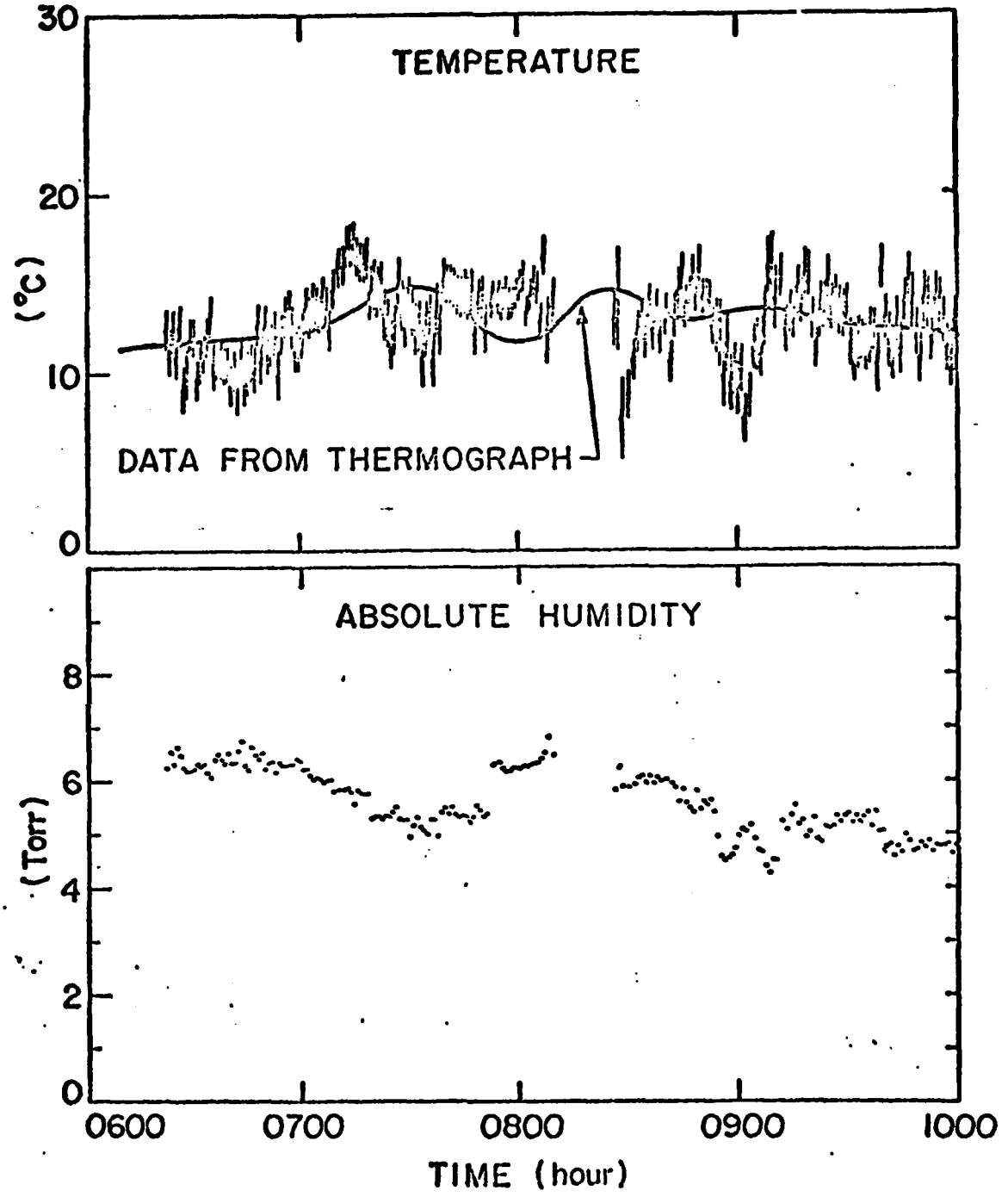

Fig.10 Temperature and absolute humidity vs. time. Measurement from morning of 11th march 1980. Temperature data are compared with record from thermograph at receiving telescope.

APPENDIX B

GROWTH OF HIGH PHASEMATCHED TEMPERATURE $LiNbO_3$ SINGLE CRYSTALS AND APPLICATION TO EFFICIENT SECOND HARMONIC GENERATION OF Nd:YAG

Robert L. Byer and Yong Kwan Park
Edward L. Ginzton Laboratory

and

Robert S. Feigelson and Wayne L. Kway
Center for Materials Research
Stanford University
Stanford, California 94305

I. INTRODUCTION

Optically induced refractive index damage in $LiNbO_3$ has been known for over ten years.[1] When $LiNbO_3$ crystals are used in nonlinear devices involving second harmonic generation (SHG) refractive index changes are induced which greatly reduce the conversion efficiency and, therefore, the usefulness of the material. The large nonlinearity of $LiNbO_3$ along with its ability to achieve non-critical phasematched SHG of the Nd:YAG laser wavelength at 1.064 μm^2 has led to considerable effort to overcome the induced refractive index damage.

It was experimentally discovered that the optical index damage in $LiNbO_3$ crystals is annealed at temperatures above approximately 170 - 200°C.[1,3-5] Therefore, if $LiNbO_3$ is grown such that the phasematching temperature is above the annealing temperature the index of refraction damage is essentially eliminated and efficient SHG of Nd:YAG is possible.

Fay et.al.,[6] and Bergman et.al.,[7] reported that the phase-matching temperagure of $LiNbO_3$ could be increased by increasing the Li_2O concentration in the melt. They showed that the SHG phasematching temperature for 1.06 μm could be increased from 4°C for congruently grown crystals with 48.6 mole % Li_2O to greater than 180°C for 54 mole % Li_2O. However, it was also found that the Li_2O concentration and thus SHG phasematching temperature in the crystal varied along the crystal growth axis for growth conditions away from the congruent melt composition.[5] Congruently grown crystals do not exhibit this variation.[8]

The cause of optical index damage in $LiNbO_3$ has been extensively studied not only because it is detrimental for nonlinear optical applications,[9 - 13] but also because it can be used as a basis for volume holographic storage.[4, 14 - 16]

Chen[4] porposed that the index damage was due to a modulation of the index of refraction via the electro-optic effect. The electric field was generated by an internal space-charge due to the drift of photo-excited electrons from the region of high light intensity to trap sites in the area of low light intensity. Johnston[17] later modified Chen's model by proposing that the internal field in the crystal could be due to the change in spontaneous polarization in the illuminated region as a result of charged lattice defects and that the divergence of the polarization was the source of the electric field. The defect in $LiNbO_3$ was identified as Fe^{2+}

impurity ions present in nominally pure crystals and the optical index damage was attributed to the Fe^{2+} to Fe^{3+} reduction.[17-20]

This model led to efforts to eliminate iron impurities in $LiNbO_3$ and thus to eliminate or reduce the magnitude of the optical index damage. It was found, however, that even very pure $LiNbO_3$ crystals showed optical damage. In an extension of the above model, Zverev et.al.,[21,22] suggested that the reduction of niobium in the crystal could account for residual index of refraction damage for even pure crystals. However, it was expected that the annealing temperature should be lower due to the smaller trapping energy of the reduced niobium site compared to the iron site.

The efforts to reduce or eliminate the index damage effect while maintaining crystal optical quality included both the reduction of the iron impurity concentration[18] and the growth of the high phasematching temperature $LiNbO_3$ (hot phasematching $LiNbO_3$) from special melt compositions. Bridenbaugh et.al.,[23] showed that MgO could be used as a co-dopant along with Li_2O to raise the phasematching temperature and simultaneously to compensate for excess Li_2O segregation. However, it was found that the effect of MgO appeared to saturate near 1.0 mole %. Another suggested approach was to grow $LiNbO_3$ at the congruent melting point in order to maintain crystal homogeniety and then to diffuse lithium into the single crystal to increase the phasematching temperature.[24-26]

After a careful review of the earlier $LiNbO_3$ crystal growth studies, we initiated a program to grow hot phasematched $LiNbO_3$ crystals with high optical quality for efficient SHG of the 1.064 μm Nd:YAG wavelength. The program had the following objectives: i) to grow $LiNbO_3$ with excess Li_2O co-doped with MgO to arrive at a composition that yielded high optical quality crystals with a phasematching temperature in excess of 180°C ; ii) to vary the growth parameters including temperature gradients, pull rate, and rotation rate to obtain optimum crystal quality; iii) to re-examine the optical damage annealing temperature to re-define the minimum allowable phasematching temperature; iv) to test crystals to correlate SHG nonlinear conversion efficiency with growth parameters; and v) to optimize and define an optimum growth process for the production of hot phasematching $LiNbO_3$ crystals for device applications.

II. CRYSTAL GROWTH PROCEDURES

Crystal growth was carried out by the standard Czochralski technique for $LiNbO_3$ utilizing an RF induction furnace. The furnace set up is shown in Fig. 1. The platinum crucible used was either 2" dia. by 2" high or 2½" in dia. by 2½" in height. The charge size ranged between 259 g and 280 g for the former and 510 g to 580 g for the latter. The growth parameters which differed from those for standard $LiNbO_3$ were mainly the pull rate and the rotation rate.

For the present testing and immediate device application the crystal samples were fabricated with cross-sections of 5 mm square and with lengths of 1 cm minimum oriented with the long axis perpendicular to the crystal optic axis. This means that the crystals could be grown in either the a- or the c- direction. However, the a-axis grown crystal proved to be less desirable because of larger compositional variations and resultant lower optical quality. Thus the c-axis was chosen as the standard growth axis in this investigation.

The selection of temperature gradients, pull rate, and crystal rotation rates is commonly governed by the melt composition and growth interface morphology. Since the crystals were grown from melts containing excess Li_2O, interface partitioning and build-up was expected. To prevent breakdown and constitutional supercooling, both axial and radial temperature were interested and the growth rates used were decreased. For the present system, the temperature gradients necessary for stable growth were regulated by both the RF coil position and an after-heater where the temperature was set at 800°C, such that the temperature increases below the melt surface and decreases along the radial direction in the melt surface. The pull rates used were from 1.6 - 4.3 mm/hr, which resulted in growth rates of approximately 1.8 - 5.0 mm/hr. The crystal rotation rates were varied between 10 and 50 rpm. Since varying the pull rate and rotation rate modified the interface shape and thus the temperature gradient and compositional characteristics

of the crystal and, therefore, the resultant optical quality, the rotation and pull rate changes were made together.

Crystal quality evaluation was based on SHG conversion efficiency tests, phasematching temperature, and optical homogeniety. These optical tests were correlated with the interface shape which, in turn was correlated with the pull rate and crystal rotation rate.

The optimum results were obtained on crystals with a planar interface grown with a pull rate of 1.6 mm/hr and a crystal rotation rate of 50 rpm. Under these conditions the SHG vs temperature phasematching curve showed a clean single peak with a width of 0.5°C, and a conversion efficiency of 35%. The crystal contained essentially no striations or banding and had an undistorted isogyre pattern indicating few optical inhomogenienties.

The most important aspect in this investigation was determining the most appropriate melt-composition to yield a high phasematched temperature, good optical quality and compositionally uniform crystal. Raising the phasematching temperature was based on the incorporation of 48.6 mole % Li_2O. Crystals were, therefore, grown from melts containing Li_2O much in excess of the congruent composition. Furthermore, MgO was added to the melt so that an excess amount of Li_2O would be incorporated into the crystal.

As shown by the phase diagram in Fig. 2 and previous work,[5] Li_2O in excess of the congruent composition is incorporated in the crystal according to the equilibrium distribution coefficient

$$k_o(\text{Exc. } Li_2O) = \frac{C_{S(\text{Exc. } Li_2O)}}{C_{L(\text{Exc. } Li_2O)}} = 0.3 \qquad (1)$$

Of course, the actual incorporation is a function of the growth parameters involved. The segregation of excess Li_2O and melt composition variation during growth and consequently the phase-matching temperature variation along the length of the crystal is large as governed by the equation for normal freezing,

$$C_s = kC_o(1-g)^{k-1} \qquad (2)$$

where C_s is the concentration of a component in the solid, C_o the concentration in the melt, k the distribution coefficient, and g the fraction solidified. As mentioned before, the addition of MgO to the melt, results in an excess amount of Li_2O over the congruent composition in the crystal. As pointed out by Bridenhaugh,[27] an addition of 1 mole % MgO to the melt results in the initial $LiNbO_3$ composition containing 0.6 mole % excess Li_2O Since the distribution coefficient for MgO in $LiNbO_3$ is 1.3, it is being rapidly depleted from the melt as the crystal is grown.

Since the excess Li_2O is determined by the M_gO concentration, the contribution for M_gO decreases in its concentration in the melt decreases. The Li_2O concentration in the crystal, which is due to excess Li_2O added to the melt, increases as growth proceeds and because of these two compensating effects, a flat Li_2O profile along the crystal length results.

The amount of excess Li_2O and MgO to be added to the melt for the desired phasematching temperature as based on available literature data. From the results of Bergman et.al.,[7] and Fay et.al.,[6] the slope of the phasematching temperature vs excess Li_2O was determined. Together with MgO doping experiment, done at Stanford and those reported by Bridenbaugh,[23,28] extrapolated curves were plotted to estimate the initial melt compositions. Crystals were grown from Li_2O-rich melts at different Li_2O concentrations with MgO doping ranging from 1.0 to 2.5 mole %. Early results showed that MgO did not contribute to increasing the phasematching temperature beyond 1.0 mole %. Consequently the MgO doping was kept at 1.0 mole % for all experimental runs with different Li_2O concentrations . The results were generally predictable with respect to the phasematching temperature vs concentration and fitted closely the initially extrapolated curves. The proper Li_2O concentration to achieve a phasematching temperature of 180°C along with a fixed 1.0 mode % MgO concentration was determined. The Li_2O concentration vs phasematching temperature is shown in Fig. 3.

Aside from the growth problems, poling is difficult in hot phasematch crystals. As the phasematching temperature reaches 180°C or above, the margin of error for poling temperature is only 20°C. At too low a temperature the crystal will not be completely poled and if too high the crystal will melt. For these reasons it is desirable to go to a lower phasematch temperature where both growth and poling can be carried out with greater ease.

Although no attempt has been made in the reduction or elimination of the Fe^{+2} impurity, the re-evaluation of the self-annealing temperature was carried out because it was believed that the $LiNbO_3$ crystals grown at Stanford have been handled with great care to achieve low impurity content. The measurements showed that the self-annealing temperature was indeed at an unexpected low value of about 120°C. With this information, crystals were grown with the new phasematching temperature target of 120°C - 130°C.

The crystals with phasematching at about 120°C showed all parameters to be as good as or better than the high phasematch crystals produced earlier. The growth procedures were thus finalized for producing crystals with the target phasematching temperature of 130°C. The following is the summary of procedures for the routine production and testing of high phasematch $LiNbO_3$ crystals for high power laser applications.

The starting materials were high purity Li_2CO_3 Nb_2O_5, and MgO. They were weighed out in the proper proportion to yield the composition of .505 Li_2O, .495 Nb_2O_5 and 1.0 mole % MgO,

for a phasematching temperature of 130°C, well mixed, and melted down in a platinum curcible utilizing a low temperature gradient furnace. Generally, the reaction and melt down is carried out in a box type of SiC furnace heated at a rate of approximately 300°C/hr to 1,280°C and soaked at that temperature for thirty minutes. At the end of the cycle the furnace was shut down and the material was allowed to cool in the furnace to room temperature. This procedure was repeated until the crucible was filled at 260-280 for the 2" crucible and 560 - 580 for the 2½" crucible.

Crystal growth was accomplished in an RF induction heated furnace with the platinum curcible as susceptor. The furnace was set up with the proper size coil and alumina parts for either the 2" dia. by 2" height or 2½" dia. by 2½" height crucible. Together with an after-heater maintained at 800°C, the coil, crucible, and furnace parts were positioned and adjusted to produce positive temperature gradients in the furnace with radial gradient of +5°C from center to edge at the melt surface. Crystal growth was commenced with a c-axis seed, allowed to come out to a proper diameter and proceeded with that diameter until a desired length was reached. During the growth cycle, the temperature was controlled at a programmed cooling rate of 5 - 7°/hr. for shouldering and a rate of .2 - 1°/hr. for the body of the crystal. At the end of the growth cycle, the crystal was tapered off by heating rapidly at 10 - 20°/hr, pulled into the after-heater, and heated to 1,100°C.

With the main furnace power (RF) turned off slowly (taking about thirty minutes), the crystal was cooled in the covered after-heater to room temperature at a rate of 100°/hr.

The poling was accomplished with a flat temperature profile tubular SiC furnace. The crystal was prepared for poling by cutting off the ends and attaching the platinum electrode with platinum paste. The crystal was placed in the furnace with leads attached, was heated up to 1,170°C at 200°/hr, and at that point, the poling field was applied. The poling voltage was adjusted for 2 V/cm and the temperature was maintained at 1,200°C for a period of two hours. At the end of this period the temperature was lowered at a moderate rate from 1,200°C to 1,100°C in fifteen minutes. At that point the poling field was turned off and the furnace temperature was programmed to lower at a rate of 100°/hr all the way to room temperature. During the entire poling cycle oxygen flow was maintained. The flow rate was 3 cfh from room temperature to 1,170°C, 2 cfh for poling and 3 cfh from 1,200°C to room temperature. When the crystal was removed from the furnace after poling, the electrodes were stripped and the ends were re-cut and polished. The Domain structure was checked by etching the crystal in a 3 : L HNO_3/HF solution at approximately 70°C for thirty minutes. By examing the etched surfaces under a microscope, the ferro-electric domain pattern was revealed. If the crystal still contained multi-domain structure, the poling cycle was repeated. In some cases higher voltage or longer poling

time was used. If the crystal was completely poled and showed a good distortion-free optical isogyre pattern, it was ready for fabrication and testing. Figure 4 shows photographs of boules 515 and 528 which were grown and poled by this procedure.

III. CRYSTAL EVALUATION

It was realized at the outset of this program that progress in the growth of hot phasematching $LiNbO_3$ crystals would depend upon rapid testing and evaluation. In addition to optical quality evaluation, each boule was tested by SHG using a cw lamp pumped, acousto-optically Q-switched Nd:YAG laser. The temperature phase-matching curve was obtained and the SHG efficiency was measured when appropriate.

Initially crystals were prepared with phasematching temperatures at or above the expected annealing temperature range of 180 - 200°C. Table 1 summarizes crystal parameters for a set of hot phasematching crystals initially tested. Among the crystals in Table I, crystal #515 shows the expected high phasematching temperature and single narrow phasematching peak as shown in Fig. 5a. The reasonably good optical quality of crystal #515 was also verified by SHG conversion efficiency results. However, the phasematching temperature of the crystal increased by 10°C from the seed to the bottom end of the boule.This result was consistent with an earlier report[6] and implied an inhomogeneous lithium concentration along the crystal growth axis.[5,6,7]

TABLE I

$LiNbO_3$ Crystal Parameters for the Phasematching Temperature Greater than 160°C

Crystal boule number	Melt composition		Pull rate (mm/hr)	Rotation rate (rpm)	Growth axis	Crystal length (mm)	Near seed		Near bottom	
	Li_2O (Mole %)	MgO (Mole %)					T_{pm} (°C)	ΔT (°C)	T_{pm} (°C)	ΔT (°C)
503	51.8	2.0	4.2	10	a	15	162	2.5	174	3.0
508	52.5	2.5	3.9	25	a	14	158	2.0	163	0.6
512	53.7	1.0	1.7	25	a	10	~176*	0.5	~178*	0.5
515	54.0	1.0	1.6	25/50+	c	10	175	0.7	184	0.7
528	54.0	1.0	1.6	25/50+	c	10	-	-	198.5	0.6

*The phasematching temperature tuning curve consists of multiple peaks.

+25 rpm from start to shoulder and 50 rpm for body of the crystal.

Crystal #528 was an attempt to duplicate crystal #515. The phasematching temperature tuning curve shown in Fig. 5b and the SHG conversion efficiency of crystal #528 showed comparable optical quality with that of crystal #515. However, the discrepancy in phasematching temperature from crystal #515 indicated that the duplication of hot phasematching $LiNbO_3$ crystals has not been consistently obtained mainly due to the difficulty involved in growing these crystals from the highly non-congruent melt.

Another suggested hot phasematching crystal preparation approach was the growth and indiffusion of $LiNbO_3$. This approach was briefly attempted for some crystals. The crystals were grown at the congruent melting point and then were diffused with 55 mole % Li_2O mixture powder at 1100°C for five or ten hours. The crystals showed significant increase of the phasematching temperature but severe deterioration of the optical quality.

Following the initial growth of high phasematching temperature crystals a re-evaluation of the annealing temperature was undertaken to attempt to define an optimum phasematching condition. The annealing tests were accomplished with a high average power cw argon ion laser operating at 0.5145 μm which is near the 0.532 μm second harmonic wavelength of Nd:YAG

The optical damage was observed in two ways; by the distorted beam shape of the transmitted beam for a preliminary observation; and by the dynamic light scattering pattern of the transmitted beam for a quantitative measurement. Both effects were caused

by the optical index damage of the crystal due to the incident .5145 μm beam. In the preliminary observation the distorted transmitted beam was imaged on polaroid film at various crystal temperatures. Consistent with the earlier reports,[4,7] we have observed that index damage occurred much more severely on the extraordinary refractive index (n_e) than on the ordinary refractive index (n_o). Thus the measurement of the beam distortion due to the index damage was made mainly for n_e wave. As an example, Fig. 6 shows the evolution of the beam distortion for crystal #528. It demonstrates that the beam distortion, in turn optical index damage, is eliminated at the unexpectedly low crystal temperature of approximately 120°C. Other recently grown $LiNbO_3$ crystals showed similar results. However, crystals grown pproximately ten years earlier showed annealing temperatures near the expected 170 - 180° range.

To measure the annealing temperature of the crystals more accurately under high power density conditions, the cw .5145 μm beam was focused very tightly into the crystal and the scattered light pattern of the transmitted beam was observed on the screen. The transmitted beam initially showed a dynamic scattered light pattern at low crystal temperatures. An increase of the crystal temperature changed the dynamic light scattering pattern to a static light scattering pattern because of the self-annealing of the optical index damage. The temperature at which the dynamic pattern changed into the static pattern was defined to be the optical index damage annealing temperature. The annealing temperatures were measured for both the 0.488 and 0.5145 μm argon ion laser lines. The annealing temperature

difference was negligibly small as observed in previous reports. Since the index damage is reduced for longer wavelengths [29] it is reasonable to consider that the annealing temperature at .5145 μm and at .5320 μm are similar.

Figure 7 shows a plot of the annealing temperature vs incident power density for a hot phasematching $LiNbO_3$ crystal #528 and a congruently grown $LiNbO_3$ crystal. Other hot phasematching $LiNbO_3$ crystals showed the similar results. Although the required annealing temperature of the hot $LiNbO_3$ crystal is increased as the incident power density increases, it saturates at a 0.1 MW/cm^2 power density and eventually clamps strongly below approximately 110°C up to 1.2 MW/cm^2 power density. Furthermore, the extrapolation of the plot shows that the crystal temperature of 120°C should be high enough to anneal the index damage even at higher power densities. Therefore, contrary to the earlier $LiNbO_3$ crystals which showed annealing temperatures near 170°C, the recently Stanford grown hot phasematching $LiNbO_3$ crystals show lower annealing temperatures of 120°C. The low annealing temperature is consistent with an extremely low Fe^{2+} impurity concentration of 1 ~ 2 ppm in the Stanford crystals.[16-20]

The discovery of the low 120°C annealing temperature immediately led to the growth of crystals with phasematching temperatures just above that value. The lower annealing temperature allowed a reduction of the excess lithium in the melt and thereby greatly lessened the growth difficulty and enhanced the possibility for growth of larger high optical quality crystals needed for efficient SHG.

Table II lists the good optical quality hot phasematching $LiNbO_3$ crystals grown at Stanford whose phasematching temperatures were lower but still high enough to anneal the optical index damage produced by the generated second harmonic of the 1.06 μm beam at approximately 20 MW/cm^2 peak power density. The second harmonic phasematching curves of crystals #557 and #558 are shown in Fig. 8 . Among the crystals listed, crystal #557 shows the lowest phasematching temperature. It also shows that the inhomogeneity of the lithium concentration along the crystal growth axis is greatly reduced since the phasematching temperature variance from the seed to the bottom end of the boule is decreased from 10°C for the previously grown hot $LiNbO_3$ crystals to 2°C for crystal #557. Crystal #558 is an attempt to duplicate the crystal #557 and shows that a consistent duplication with high optical quality is indeed possible at this melt composition. The 2 ~ 3° C phasematching temperature difference between two crystals is mainly due to the SHG temperature measurement error of the crystal oven controller.

In addition to complete index damage annealing and the low Li_2O composition inhomogeneity, the high optical quality of these crystals is supported by high SHG conversion efficiency. The SHG conversion efficiency of the crystals was measured by both TEM_{oo} mode and multi-transverse mode beam from the 1.06 μm Nd:YAG source. When a TEM_{oo} mode beam with 3 watts average power and 1 KHz pulsed Q-switch repetition rate was focussed into the

TABLE II

$LiNbO_3$ Crystal Parameters for the Phasematching Temperature Greater than 120°C

Crystal number	Melt composition		Pull rate (mm/hr)	Rotation rate (rpm)	Growth axis	Crystal length (mm)	Near seed		Near bottom	
	Li_2O (Mole %)	MgO (Mole %)					Tpm (°C)	ΔT (°C)	Tpm (°C)	ΔT (°C)
543	51.5	1.0	1.6	50	c	10	145.5	0.9	149.0	0.8
549	51.5	1.0	1.6	40	a	10	151.3	0.7	155.9	0.7
554	50.6	1.0	1.6	20	a	10	128.6	1.0	131.6	0.8
557	50.5	1.0	1.6	50	c	20	117.5	0.4	119.2	0.4
558	50.5	1.0	1.6	50	c	20	118.7	0.4	123.2	0.5

2 cm length crystals at approximately 20 MW/cm^2 peak power density, the crystals showed a 40% average power conversion efficiency.

A 10 mrad divergence multi-transverse mode beam with the same peak power density level produced a 33% average power conversion efficiency. The acceptance angle of a 2 cm long $LiNbO_3$ crystal is calculated to be 15 mrad.[31] The comparable SHG conversion efficiency of the crystals for the multi-transverse mode to that for the TEM_{oo} mode verifies that advantage of non-critical phasematching is fully utilized.

The measurements of phasematching temperature tuning curves, annealing temperatures, phasematching temperature variance along the crystal growth axis, and SHG conversion efficiency demonstrates that high quality hot phasematching $LiNbO_3$ crystals can be grown with consistent SHG performance.

IV. CONCLUSION

During the course of this program, we have demonstrated that hot phasematching $LiNbO_3$ crystals can be grown with the optical quality, reproducibility and size required for device applications by the proper choice of composition and growth parameters.

More significantly and specificially, we have demonstrated that $LiNbO_3$ crystals with a phasematching temperature greater than 180°C can be grown with small concentration gradients from a melt doped with MgO and excess Li_2O together with a planar growth interface; that the phasematch temperature can be readily

adjusted simply by changing the excess Li_2O concentration proportional to the phasematch temperature desired; that the crystal quality and SHG characteristics can be maintained as long as the MgO concentration and growth parameters are held constant. We have also found that the self-annealing temperature is much lower, near 120°C for the Stanford grown crystals, as compared to the previously reported value of 170 - 180°C.

Taking advantage of the lower self-annealing temperature, the crystals grown with phasematching temperature of approximately 120°C showed exceptional optical homogeneity, and a 40% average power SHG conversion efficiency.

The improved hot phasematching $LiNbO_3$ crystals along with the electro-optical or piezo-optical compensation for self heating effects[32] should greatly enhance crystal device applications to high average power second harmonic generation of the Nd:YAG source.

ACKNOWLEDGEMENT

We want to acknowledge the support provided by the Department of Energy through contract #LLL 3488009.

REFERENCES

1. A. Ashkin, G.D. Boyd, J.M. Dziedzic, R.G. Smith, A.A. Ballman, J.J. Levinstein and K. Nassau, "Optically Induced Refractive Index Inhomogeneities in $LiNbO_3$ and $LiTaO_3$", Appl. PHys. Letts. 9(1), p.72-74 (1966).

2. G.D. Boyd and A. Ashkin, "Theory of Parametric Oscillator Threshold with Single Mode Optical Masers and Observation of Amplification in $LiNbO_3$", Phys. Rev. 146(1), p.187-198 (1965).

3. J.E. Midwinter, "Assessment of LIthium-Meta-Niobate for Nonlinear Optics", Appl. Phys. Letts. 11(4), 128-130 (1967).

4. F.S. Chen, "Optically Induced Change of Refractive Indices in $LiNbO_3$ and $LiTaO_3$", Jounr. Appl. Phys. 40(8), p.3389-3396 (1969).

5. J.R. Carruthers, G.E. Peterson and M. Grasso, "Non-stoichiometry and Crystal Growth of Lithium Niobate", Journ. Appl. PHys. 42(5), p.1846-1851 (1971).

6. Homer Fay, W.J. Alford and H.M. Dess, "Dependence of Second Harmonic Phasematching Temperature in $LiNbO_3$ Crystals on Melt Composition", Appl. Phys. Letts. 12(3), p.89-92 (1968).

7. J.G. Bergman, A. Ashkin, A.A. Ballman, J.M. Dziedzic, H.J. Levinstein and R.G. Smith, "Curie Temperature, Birefringence and Phasematching Temperature Variation in $LiNbO_3$ as a Function of Melt Stoichiometry", Appl. Phys. Letts. 12(3), p.92-94 (1968).

8. R.L. Byer, J.F. Young and R.S. Feigelson, "Growth of High Quality $LiNbO_3$ Crystals from the Congruent Melt", Journ. Appl. Phys. 41(6), p.2320-2325 (1970).

9. J.E. Midwinter, "Lithium Niobate:Effects of Composition on the Refractive Indices and Optical Second Harmonic Generation", Journ. Appl. Phys. 39(7), p.3035-3038 (1968).

10. H. Tsuya, Y. Fujino and K. Sugibuchi, "Dependence of Second Harmonic Generation on Crystal Inhomogeneity", Journ. Appl. Phys. 41(6), p.2557-2563.

11. F.R. Nash, G.D. Boyd, M. Sargent III and P.M. Bridenbaugh, "Effect of Optical Inhomogeneities on Phase Matching in Nonlinear Crystals", Journ. Appl. Phys. 41(6), p.256 4-2576 (1970).

12. R.G. Smith, "Effect of Index Inhomogeneities on Optical Second Harmonic Generation", Journ. Appl. Phys. 41(7), p.3014-3017 (1970).

13. N.B. Angert, V.A. Pashkov and M.M. Solovera, "Optically Induced Inhomogeneity of the Refractive Index of $LiNbO_3$ Crystals", Soviet Physics JETP, 35(5), p.867-869 (1972).

14. D.L. Staebler and J.J. Amodei, "Coupled Wave Analysis of Holographic Storage in $LiNbO_3$", Journ. Appl. Phys. 43(3), p.1042-1049 (1972).

15. D. von der Linde, A.M. Glass and K.F. Rodgers, "Multi-photon Photo-refractive Processes for Optical Storage in $LiNbO_3$", Appl. Phys. Letts. 25(3), p.155-157 (1974).

16. Rajiv R. Shah, Dae M. Kim, T.A. Rabson and F.K. Tittel, "Characterization of Iron-doped Lithium Niobate for Holographic Storage Applications", Journ. Appl. Phys. 47(12), p.5421-5431 (1976).

17. W.D. Johnston, Jr., "Optical Index Damage in $LiNbO_3$ and Pyroelectric Insulators", Journ. Appl. Phys. 41(8), p.3279-3285 (1970).

18. A.M. Glass, G.E. Peterson and T.J. Negran, "Optical Index Damage in Electro-optic Crystals", Proceedings of the NBS Symposium on Damage in Laser Material, NBS. Spec. Publ. 372, p.15-26 (1972).

19. A. Zylbersztejn, "Thermally Activated Trapping in Fe-Doped $LiNbO_3$", Appl. Phys. Letts. 29(12), p.778-780 (1976).

20. A.M. Glass, D. von der Linde and T.J. Negran, "High Voltage Bulk Photovoltaic Effect and the Photorefractive Process in $LiNbO_3$", Appl. Phys. Letts. 25(4), p.233-235 (1974).

21. G.M. Zverev, E.A. Levchuk, V.A. Pashkov and Yu.D. Poryadin, "Laser Radiation induced Damage to the Surface of Lithuum Niobate and Tantalate Single Crystals", Soviet Journ. Quant. Elect. 2(2), p.167-169 (1972).

22. G.M. Zverev, S.A. Kolyadin, E.A. Levchuk and L.A. Skvortsov, "Influence of the Surface Layer on the Optical Strength of Lithium Niobate", Soviet Journ.of Quant. Elect. 7(9) p.1071-1075 (1977).

23. P.M. Bridenbaugh, J.R. Carruthers, J.M. Dziedzic and F.R. Nash, "Spatially Uniform and Alterable SHG Phase-matching Temperature in $LiNbO_3$", Appl. Phys. Letts. 17(3) p.104-106 (1970).

24. S. Miyazawa, R. Guglielmi and A. Carenco, "A Simple Technique for Suppressing Li_2O Out-Diffusion in Ti:$LiNbO_3$ Optical Waveguide", Appl. Phys. Letts. 31(11), p.742-744 (1977).

25. R.L. Holman, P.J. Cressman and J.F. Ravelli, "Chemical Control of Optical Damage in Lithium Niobate", Appl. Phys. Letts. 32(5), p.280-283 (1978).

26. B.U. Chen and A.C. Pastor, "Elimination of Li_2O Out-Diffusion Waveguide in $LiNbO_3$ and $LiTaO_3$", Appl. Phys. Letts. 30(11), p.570-571 (1977).

27. R.L. Byer and R.L. Herbst, private communication.

28. P.M. Bridenbaugh, "Factor Affecting the Growth of $LiNbO_3$ Useful for Nonlinear Optical Applications", Journ. Crystal Growth, 19, p.45-52 (1973).

29. H.B. Serreze and R.B. Goldner, "Study of the Wavelength Dependence of Optically Induced Birefringence Change in Undoped $LiNbO_3$", Appl. Phys. Letts. 22(12), p.626-627 (1973).

30. D. Redfield and W.J. Burke, "Optical Absorption Edge of $LiNbO_3$", Journ. of Appl. Phys. 45(10), p.4566-4571 (1974).

31. R.L. Byer and R.L. Herbst, "Parametric Oscillation and Mixing", published in Nonlinear Infrared Generation, ed. by Y.R. Shen, Springer-Verlag, p.81 (1977).

32. D.T. Hon, "Electro-optic and Piezo-optic Tuning of Second Order Nonlinear Processes in Crystals". Journ. of Appl.Phys. 49(1), p.396-402 (1978) ; "Electro-optical Compensation for Self Heating in CD*A During SHG", IEEE, Journ. Quant. Electr. QE-12(2), p.148-151 (1976).

FIGURE CAPTIONS

1. A Schematic of the $LiNbO_3$ crystal growth furnace.
   1. Alumina Pull Rod, 2. After Heater, 3. TC Signal to Aux. Controller, 4. Pt.Seed Holder, 5. $LiNbO_3$ Crystal, 6. $LiNbO_3$ Melt, 7. Pt. Crucible, 8. Alumina Plate, 9. RF Coil, 10. Alumina tubes, 11. Firebricks. 12. Sapphire Rod-Radiation Pyrometer, 13. Temp. Signal to Main Controller, 14. Fiberfrax.

2. Phase diagram of the Li_2O-Nb_2O_5 System (after Carruthers et.al.[5]).

3. Phasematching temperature vs concentration of Li_2O and MgO in the melt.

4. Photographs of high phasematching temperature $LiNbO_3$ crystals (#515 and #528). The crystal #528 is an attempt to duplicate #515. Note the solid liquid interface shape at the bottom of the boules.

5. Phasematching temperature tuning curve of the crystals from boule #515 and #528. Both were sampled at the bottom of the boules.

6. Photographs of the 0.5145 μm beam propagating as an extraordinary wave through crystal #528. The index damage is annealed at temperatures greater than 120°C.

7. Annealing temperature vs power density for 0.5145 μm incident on recently grown $LiNbO_3$ crystals.

8. Phasematching temperature tuning curve of the crystals from boules #557 and #558. Upper traces are sampled near the seed of the boules and lower ones from the bottom.

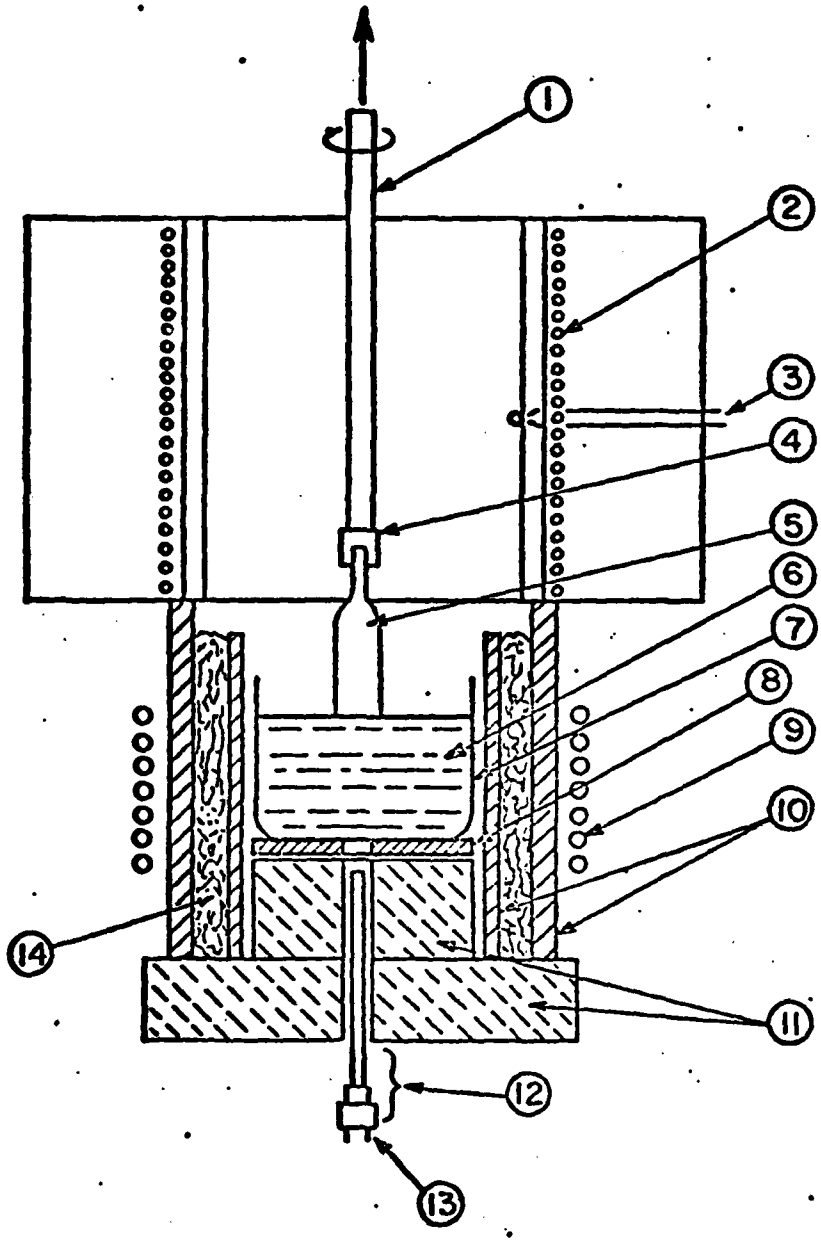

FIG. 1--A schematic of the $LiNbO_3$ crystal growth furnace.
1. Alumina Pull Rod, 2. After Heater, 3. TC Signal to Aux.Controller, 4. Pt.Seed Holder, 5. $LiNbO_3$ Crystal, 6. $LiNbO_3$ Melt, 7. Pt.Crucible, 8. Alumina Plate, 9. RF Coil, 10. Alumina Tubes, 11. Firebricks. 12. Sapphire Rod-Radiation Pyrometer, 13. Temp. Signal to Main Controller, 14. Fiberfrax.

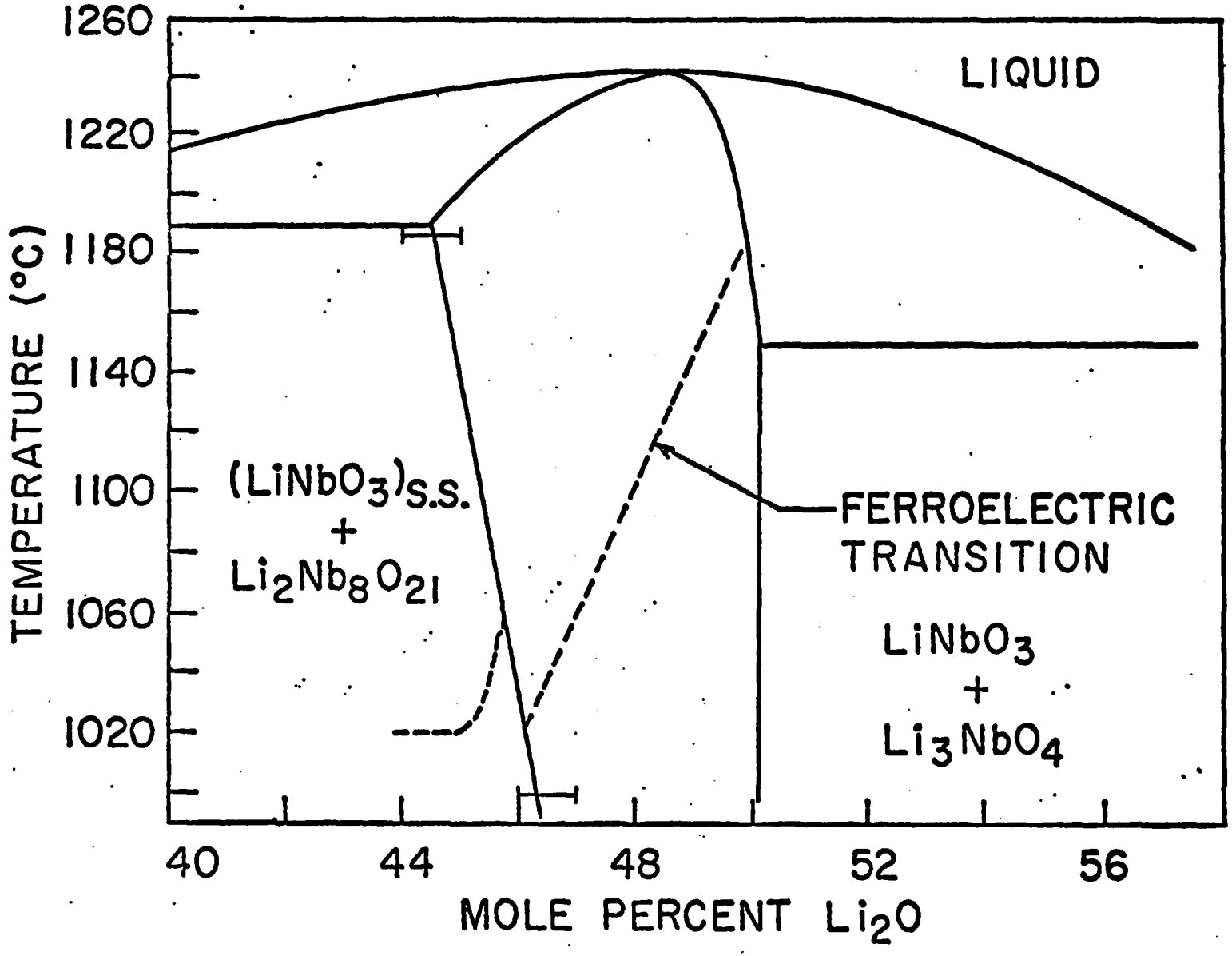

FIG. 2--Phase diagram of the Li_2O-Nb_2O_5 System (after Carruthers et.al.[5]).

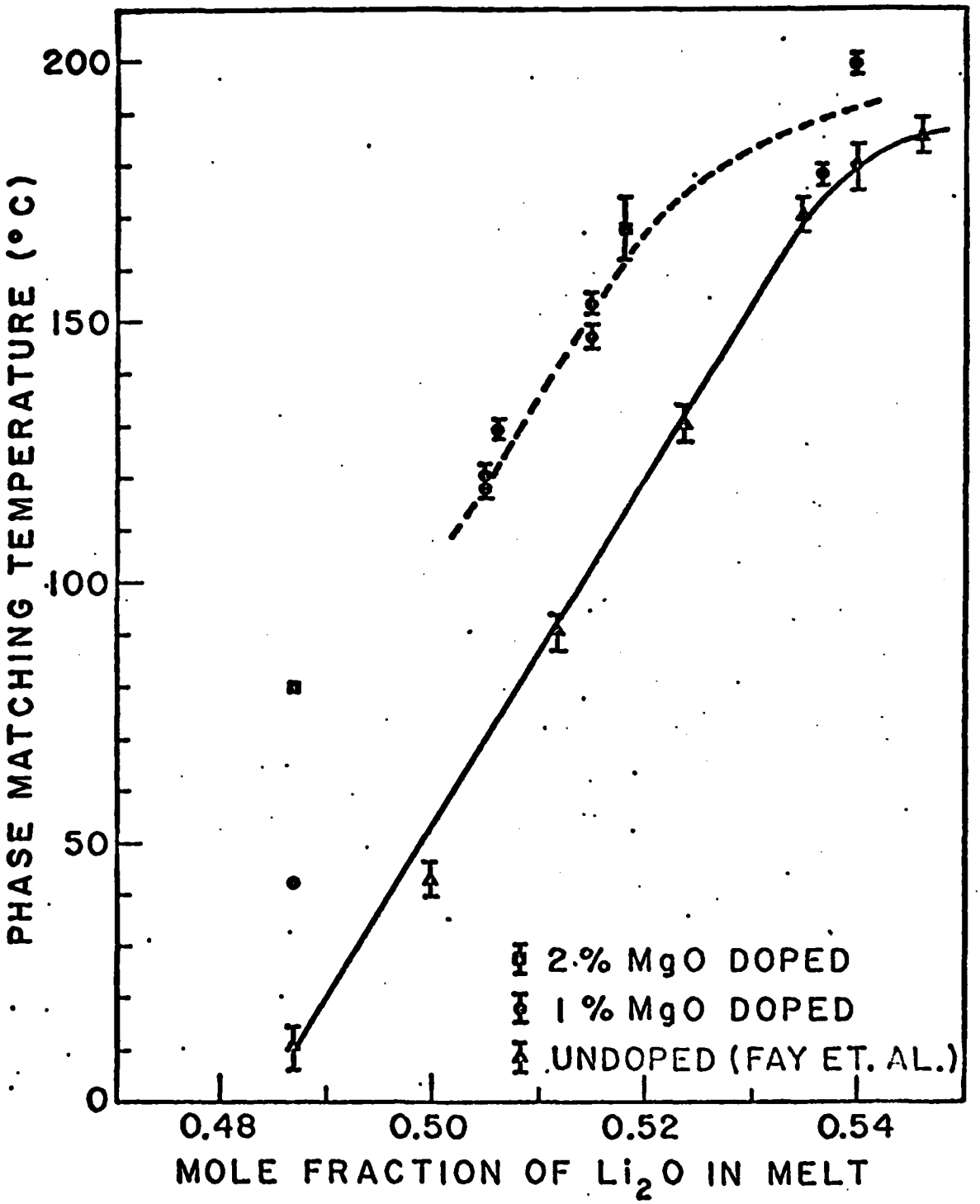

FIG. 3--Phasematching temperature vs concentration of LiO_2 and MgO in the melt.

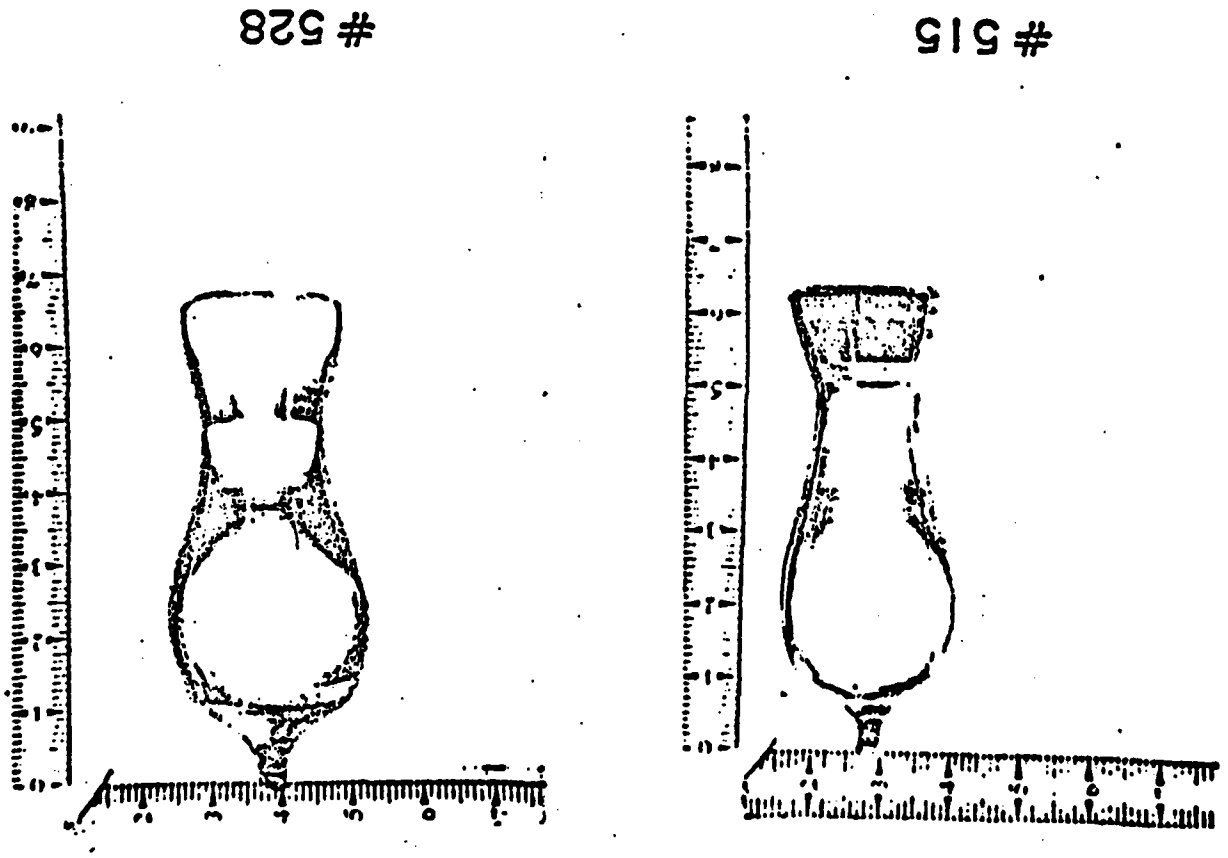

FIG. 4--Photographs of high phasematching temperature $LiNbO_3$ crystals (#515 & #528). The crystal #528 is an attempt to duplicate #515. Note the solid liquid interface shape at the bottom of the boules.

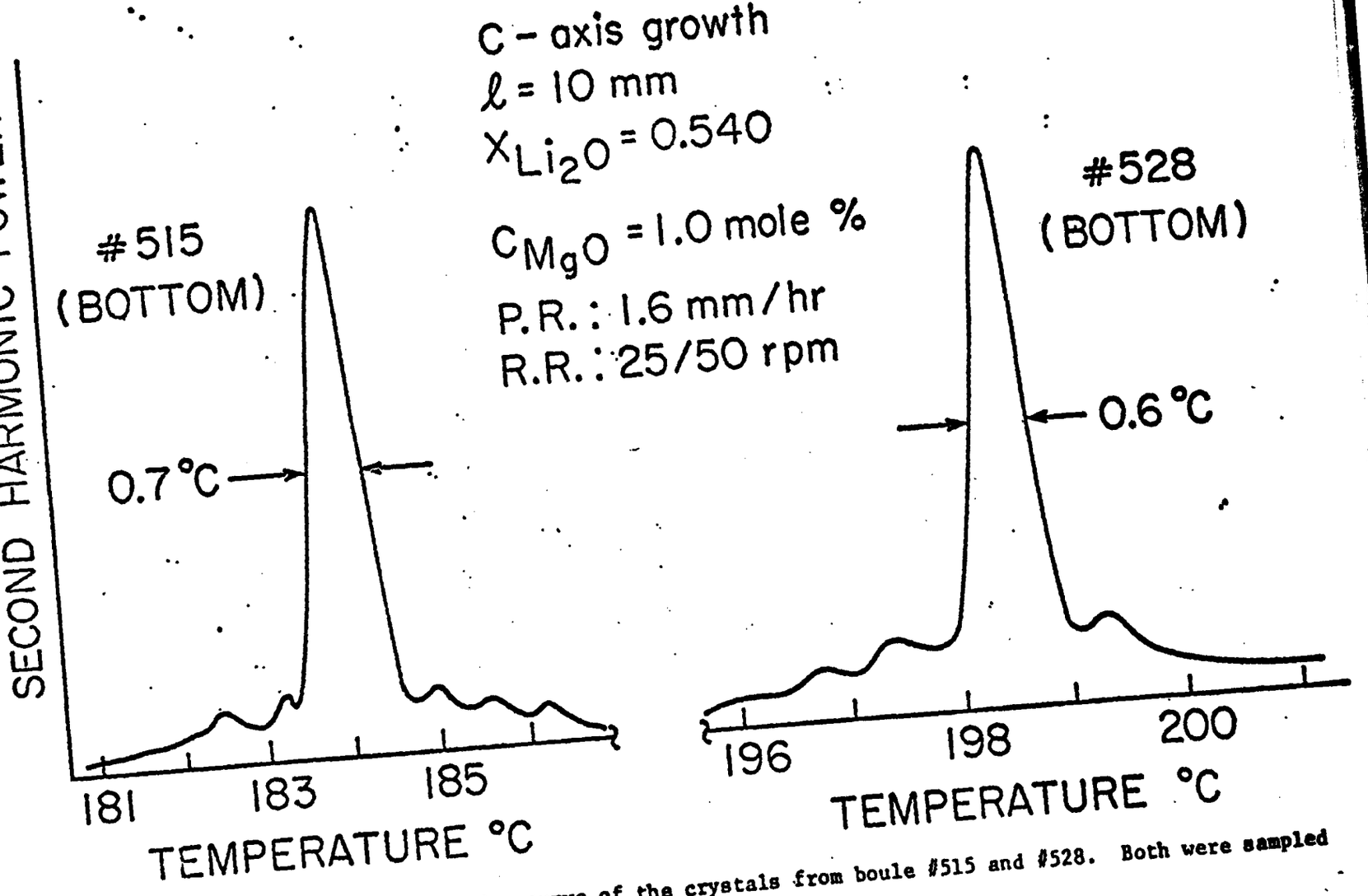

FIG. 5--Phasematching temperature tuning curve of the crystals from boule #515 and #528. Both were sampled at the bottom of the boules.

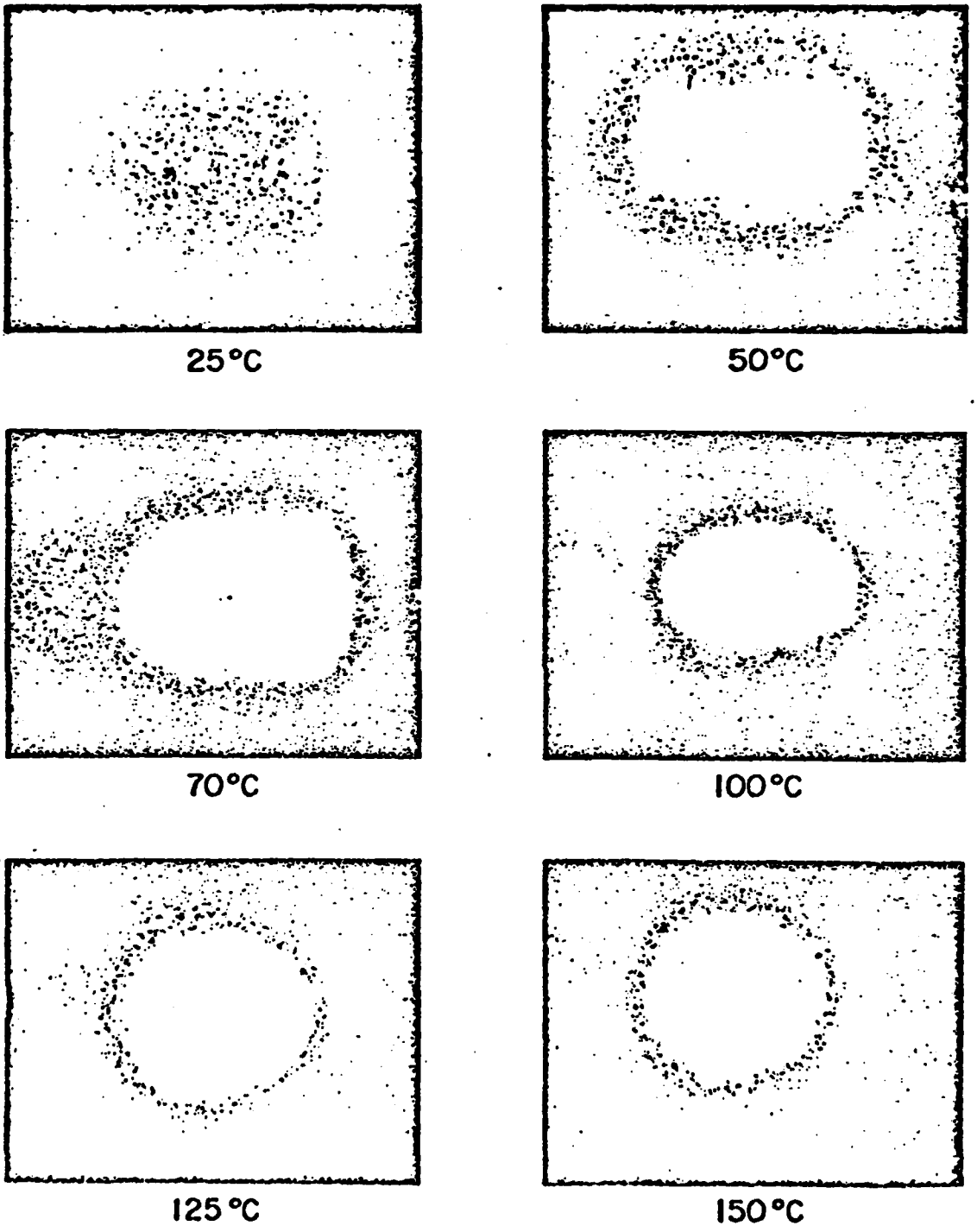

FIG. 6--Photographs of the 0.5145 μm beam propagating as an extraordinary wave through crystal #528. The index damage is annealed at temperatures greater than 120°C.

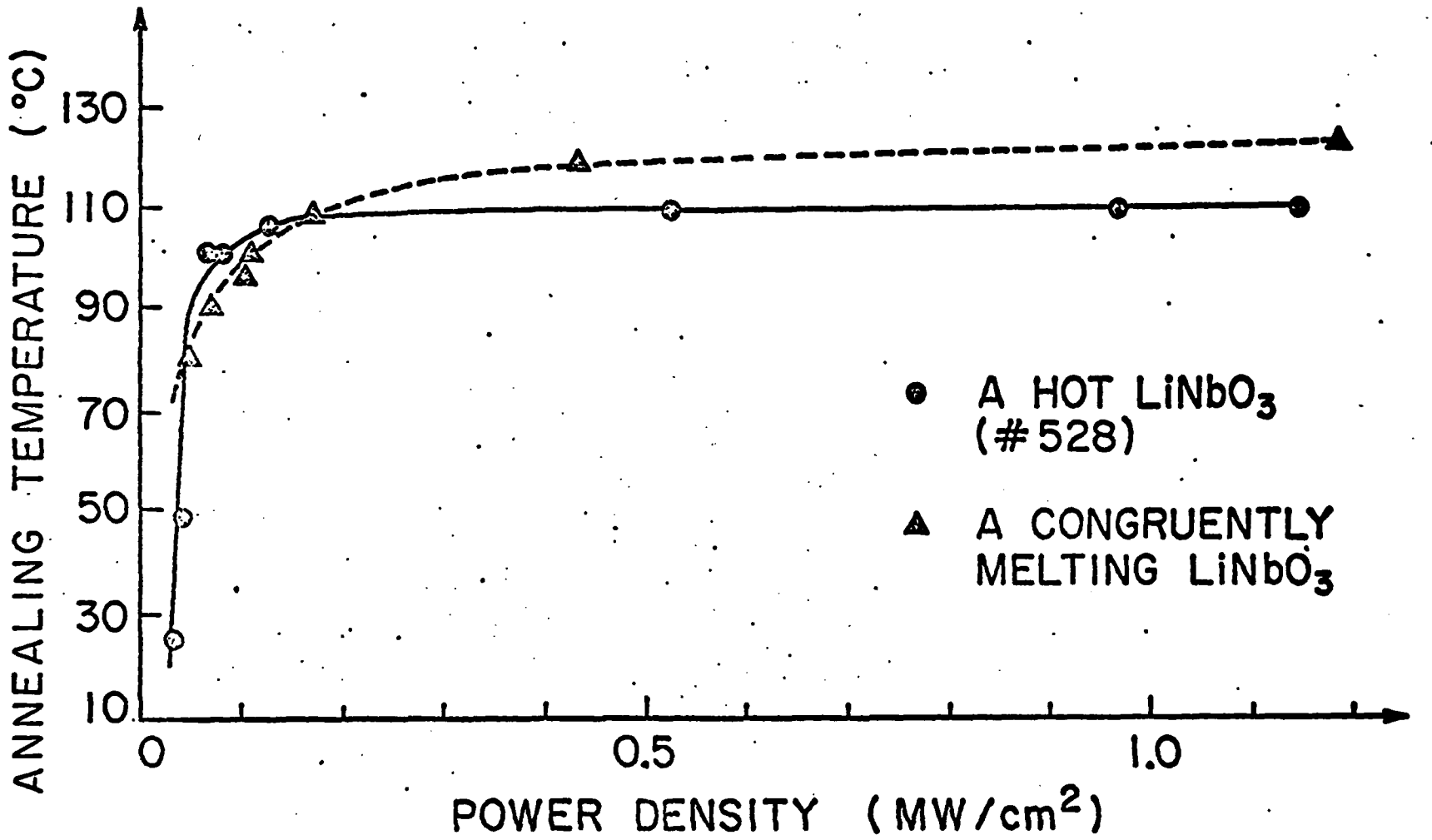

FIG. 7--Annealing temperature vs power density for 0.5145 μm incident on recently grown $LiNbO_3$ crystals.

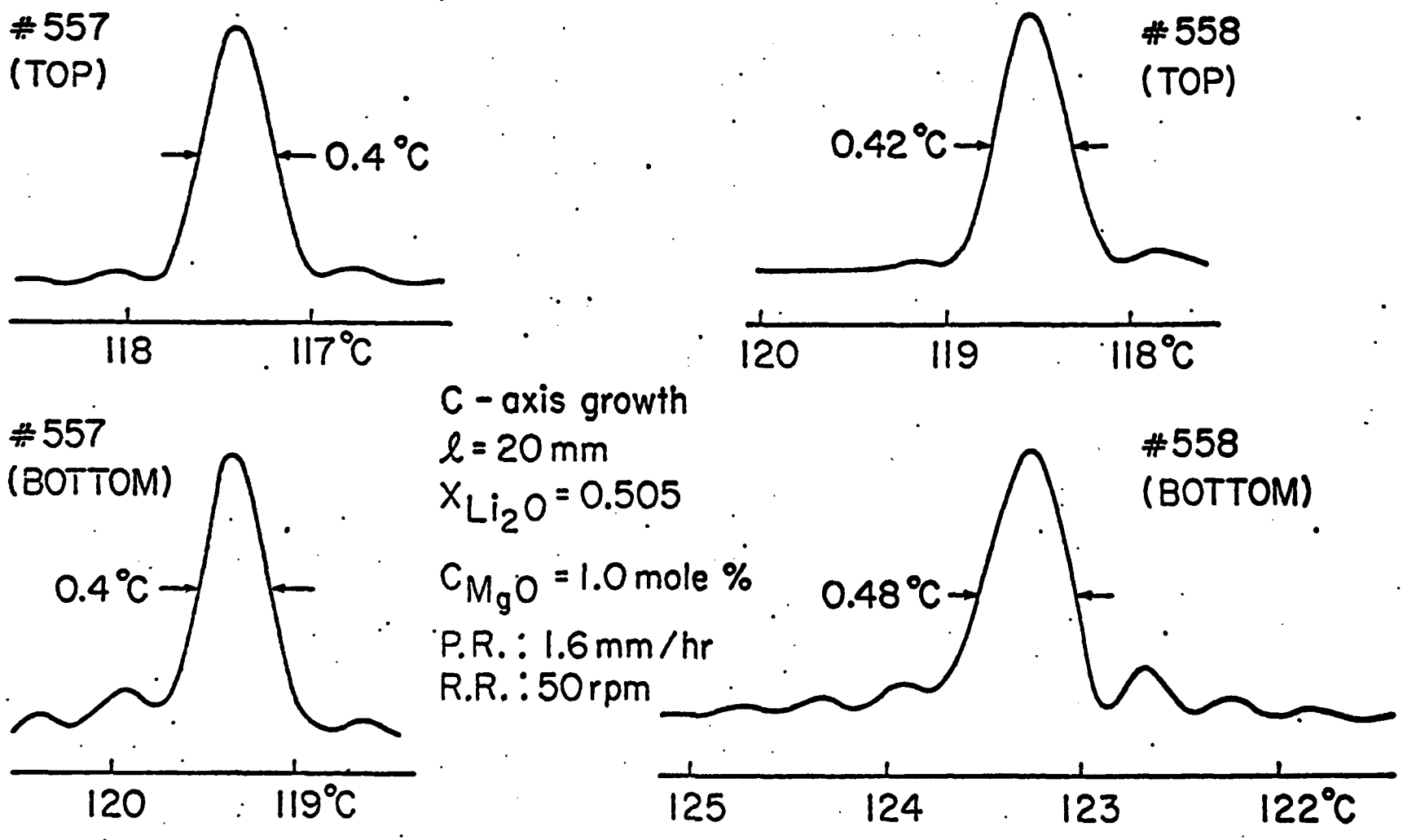

FIG. 8--Phasematching temperature tuning curve of the crystals from boule #557 & #558. Upper traces are sampled near the seed of the boules and lower ones from the bottom.